Lukas Gölles, BSc
01530006

Optimally Curved Arc Source For Sound Reinforcement

Master's Thesis

Master's Degree Programme
Electrical Engineering and Audio Engineering (UF 066 413)

Graz, University Of Technology
University Of Music and Performing Arts Graz

Supervisor: Ass.Prof. DI Dr.rer.nat. Franz Zotter
Assessor: O.Univ.Prof. Mag.art. DI Dr.techn. Robert Höldrich

Graz, March 2021

Kurzfassung

Die wichtigste Herausforderung in der Beschallungstechnik ist die gezielte gleichmäßige Versorgung von ausgedehntem Publikum mit verstärktem Direktschall. Sie wird nach Stand der Technik häufig durch progressiv gekrümmte Verkettung von Linienquellen gemeistert. Diese wird durch die Kombination einzelner im Winkel unterschiedlich geneigter Elemente an die Hörfläche angepasst. Diese Arbeit schlägt eine Differentialgleichung, die sich aus der Sattelpunktsnäherung ergibt, vor, um daraus die optimale Krümmung der Quelle bzw. die Quellform zu berechnen, die verwendet werden kann, um eine Verkettung von Linienquellen einzustellen. Der 3D gedruckte Prototyp ist für Frequenzen über $1\,\mathrm{kHz}$ geeignet und wird mit einem Kompressionstreiber betrieben. Die phasenausgeglichenen Wellen, die an der Öffnung ankommen, bilden im Wesentlichen die optimal gekrümmte Schallquelle mit optimaler Krümmung (Opimtally Curved Arc Source, OCAS). Simulationen und Messungen des Prototyps zeigen die Effektivität für höhere Frequenzen. Mit Hilfe neuester webbasierter 3D Audiowiedergabe ist es möglich ein immersives OCAS Setup virtuell zu erleben.

Abstract

Sound reinforcement typically requires the capacity to supply large audience areas uniformly with amplified direct sound. It is state of the art to employ progressively curved line-source arrays adapted to satisfy this requirement. Adaptation to the listening area is done by adjusting the angles between individual elements in the chain of line-source loudspeakers. This work suggests formalizing the optimal progression of the source curvature in terms of a differential equation resulting from the stationary phase approximation. This thesis introduce the formalism that is directly applicable to shaping line-source arrays, and a new compact prototype of the resulting optimally curved arc source (OCAS) is presented. The prototype is designed for frequencies above 1kHz, fed by a compression driver, and built as a 3D-printed waveguide. The phase-equalized waves arriving at its orifice essentially constitute the optimally curved arc source. The effectiveness of the formalism is proved by simulations and measurements of the prototype. The latest web-based 3D playback technology makes it possible to virtualize an immersive OCAS setup.

ERKLÄRUNG

Hiermit bestätige ich, dass mir der *Leitfaden für schriftliche Arbeiten an der KUG*[1] bekannt ist und ich die darin enthaltenen Bestimmungen eingehalten habe. Ich erkläre ehrenwörtlich, dass ich die vorliegende Arbeit selbständig und ohne fremde Hilfe verfasst habe, andere als die angegebenen Quellen nicht verwendet habe und die den benutzten Quellen wörtlich oder inhaltlich entnommenen Stellen als solche kenntlich gemacht habe.

Graz, den 18. März 2021 ....

(Unterschrift)

---

[1] Leitfaden für schriftliche Arbeiten an der KUG (laut Beschluss des Senats vom 18. Juni 2019)

Contents

Chapter 1

Introduction

One of the big challenges for sound reinforcement in concerts, cinema or speech events is to provide high-quality sound for the largest parts of a predefined audience area. For example, 8000 persons (4 persons per square meter) have to be provided with high-quality sound at the fairgrounds in Graz with approximately $40\,\mathrm{m} \times 50\,\mathrm{m}$ space for the audience. So far, in the typical professional sector, large-area sound systems still consider the supply with single-channel sound material fed to multiple line-source loudspeaker arrays.

These loudspeaker arrays are highly discussed in the literature. Manor presents on his webpage a basic overview on this topic [1]. Toole [2] describes the application of line sources, as well as the idea of constant direct-sound level for all listener positions. A basic work on line-source arrays is published by Heil et. al that treats sound fields created by multiple sources [3]. The related paper about Wavefront Sculpture Technology by Urban et al. [4] continues the discussion on discrete loudspeaker arrays. From a more practical view, Smith [5], Straube et al. [6] and [7] discuss the modelling and optimization of these line-source loudspeaker arrays. To guarantee constructive interference between the waves of nearby cabinets, Heil presents a waveguide in 1992 [8] that is interestingly used in L'Acoustics loudspeaker systems until now. In 2003 Vincenot and Deffarges describe the hyperbolic reflective wave source [9] that works based on the principle of reflection on a hyperbolic reflector. Another approach is given by Spillmann et al. [10] that guides the waves in different chambers while Desrosiers et al. [11] uses an interior body to guide the waves along it. What they all have in common is that their publications are aimed for large scale sound reinforcement systems primarily. Moreover there is no mathematical description of the source geometry that allows to cover the audience area with position independent direct sound levels.

In the recent past immersive playback setups gain in importance. Be it two-dimensional, like 5.1 or 7.1, or three-dimensional, for example Auro-3D, the focus in all lies on a sweet area, which is as large as possible. The properties of such sound systems are already relatively well understood, as long as the size of the audience remains manageable, i.e. less than $10\,\mathrm{m} \times 10\,\mathrm{m}$. This corresponds to an audience up to 200 with 2 seats per square meter at a cinema, the Györgi-Ligeti Hall in Graz or the Helmut List Hall in Graz. The sweet area for such playback systems was reviewed for an playback setup in [12] and [13] using Ambisonics, a scene-based method for recording and reproducing two- or three-dimensional sound fields. Newer research [14] and [15] has shown that even $2\,\mathrm{m}$ away from the center of the audience area, the sense of a fully enveloping auditory scene, for example diffuse reverberation, cannot be created. Although [16] describes a setup using point sources for large listening areas, the well-known 3D audio technology is still missing speaker systems that are adapted to the geometry, i.e. the size of the audience and that can supply the entire audience with a (nearly) constant sound level from any direction.

The first question is: Why are point-source, piston or horn loudspeakers often unable to provide a constant direct-sound level across the entire audience? To answer this question, one have a look at the amplitude behaviour of a point source over distance. In the simplest case a loudspeaker is modelled as a point source. This source is described by Green's function

$$G(R,\omega) = \frac{e^{-i\,k\,R}}{4\,\pi\,R}\ , \tag{1.1}$$

which is derived as solution of the wave equation [17]

$$\nabla^2\, G(R,\omega) + k^2\, G(R,\omega) = -\delta(\boldsymbol{r} - \boldsymbol{r}_0) \tag{1.2}$$

$$\nabla^2 = \frac{\partial^2}{\partial\, x^2} + \frac{\partial^2}{\partial\, y^2} + \frac{\partial^2}{\partial\, z^2} = \text{div grad}\,, \tag{1.3}$$

where the source is located at the position $\boldsymbol{r}_0$. Its field is evaluated at any receiver position $\boldsymbol{r}$ so that the distance R becomes $\|\boldsymbol{r} - \boldsymbol{r}_0\|$. In the equations, k denotes the wave number and ω the angular frequency. As we are interested in the dependency of the amplitude on distance, we recognize the dependency as $\frac{1}{R}$. The left plot of figure 1.1 shows the level map of a point source located at $(0|0|0)$ over an audience area of $50\,\mathrm{m} \times 40\,\mathrm{m}$, which expands over the xy plane. This area is defined in such a way that the point source lies in the middle of a boundary line. In decibels, $\frac{1}{R}$ relates that doubling the distance R yields to an attenuation of $6\,\mathrm{dB}$.

To improve the direct-sound coverage over distance, one might place multiple point sources on top of each other. Assuming the same audience area with points of observations $\boldsymbol{x}_r = \begin{bmatrix} x_r & y_r & 0 \end{bmatrix}^T$ as before, an ideal line source is considered that expands along the z axis. Placing multiple infinitesimal small point sources with infinitesimal distance on top of each other leads to an ideal line source. Its sound pressure is calculated as an integral of the Green's function over the height coordinate z,

$$p(R,\omega) = \int_{-\infty}^{\infty} G(R,\omega)\,\mathrm{d}z = \int_{-\infty}^{\infty} \frac{e^{-i\,k\,\sqrt{x_r^2+y_r^2+z^2}}}{4\,\pi\,\sqrt{x_r^2+y_r^2+z^2}}\,\mathrm{d}z\,. \tag{1.4}$$

As shown in A.1, the result of this integral is a scaled version of the Hankel function zeroth order of second kind,

$$p(R,\omega) = \frac{1}{4\,i}\, H_0^{(2)}(k\,R)\,. \tag{1.5}$$

For large R the solutions becomes a cylindrical diverging wave [17], i.e.

$$p(R,\omega) = \frac{1}{4\,i}\sqrt{\frac{2}{\pi\,k\,R}}\,e^{-j(k\,R-\frac{\pi}{4})}\,. \tag{1.6}$$

In decibels, this relates that doubling the distance R yields to an attenuation of only $3\,\mathrm{dB}$. The result is also show graphically for a line source in figure 1.1 on the right that expands along the z axis.

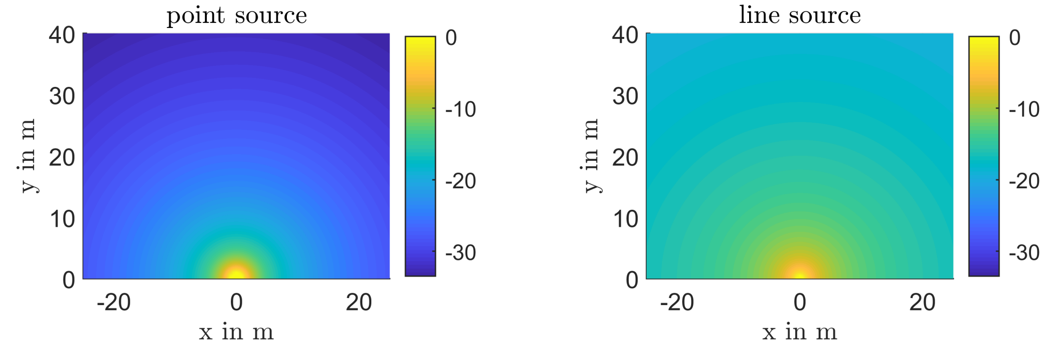

Figure 1.1 – Magnitude over an audience area on the xy plane for a single point source located at $(0|0|0)$ (left) and a line source extended along the z axis with x,y coordinates $(0|0)$.

Motivation for new source shapes. As a line source comes closer to the wishes of a (nearly) constant direct-sound level over distance, the integral of the Green's function turns out to be useful. Therefore an interesting approach will be to bend this line source as to obtain a curved continuous source capable of providing constant direct-sound levels in the audience area. Therefore the path of integration has to be found, which is an essential part of this thesis.

Structure of this thesis. Chapter 2 begins by approximating the integral over the unknown integration path to define the optimal source contour. As the resulting contour is curved or arced, the new source is called Optimally Curved Arc Source (OCAS). In addition, a waveguide is presented that allows a customisable orifice perfectly fitting the OCAS shape or parts thereof. Chapter 3 shows the advantage of the newly found shape based on numerical simulations. The simulations also show thinkable errors emerging from misplacement, either shifting or rotating. The chapter about misconfiguration describes the resulting effects. The question, should OCAS be implemented by standard components as line-source arrays or does it make sense to create custom waveguides, is also discussed in detail by considering a stereo setup and also a 3D setup. Chapter 4 shows a possible solution to replace all horizontal point-source loudspeakers at the IEM CUBE by custom DIY self 3D printed prototypes. The focus of this chapter lies on the design process as well as the evaluation based on measurements and sound examples played back by the CAT3DA player, a web-based 3D audio player, which allows user's head rotation without additional hardware. Finally chapter 5 summarizes and gives an outlook for possible further work.

Chapter 2

Theoretical Overview

2.1 Optimal Source-Contour For Optimal Coverage

To find the optimal contour of a source so that optimal coverage of a specific audience area is achieved, the sound pressure as the integral of the Green's function $G(R) = \frac{e^{-i\,k\,R}}{4\,\pi\,R}$ over the source positions $\boldsymbol{x}(s) = \begin{bmatrix} x(s) & v(s) \end{bmatrix}^T$ is considered. x denotes the horizontal axis and v the vertical axis,

$$p = \int G(R)\,\mathrm{d}s\,. \tag{2.1}$$

The integral is observed at the point $\boldsymbol{x}_r = \begin{bmatrix} x_r & 0 \end{bmatrix}^T$ that lies at a certain x coordinate geometrically below the contour to be found. By this point of observation, the distance inserted into the Green's function is

$$R = \|\boldsymbol{x} - \boldsymbol{x}_r\| = \sqrt{\left[x(s) - x_r\right]^2 + v(s)^2}\,. \tag{2.2}$$

The integral in s is now rewritten in terms of x. This can be done using the rectangular slope triangle yielding $\Delta\,v$ for a movement in $\Delta\,x$, and hence the natural length segment $\Delta\,s$ as hypotenuse along the tangent, which is then made infinitely small to re-express $\mathrm{d}s$ by $\mathrm{d}x$, as shown in Figure 2.1 geometrically,

$$\Delta\,s = \sqrt{\Delta\,x^2 + \Delta\,v^2} = \Delta\,x\sqrt{1 + \left(\frac{\Delta\,v}{\Delta\,x}\right)^2} \tag{2.3}$$

$$\mathrm{d}s = \sqrt{1 + \left(\frac{\mathrm{d}v}{\mathrm{d}x}\right)^2}\,\mathrm{d}x = \sqrt{1 + (v')^2}\,\mathrm{d}x\,. \tag{2.4}$$

The stationary phase method [18] for an integral over a phasor that oscillates rapidly along the integration path permits to relate the result of the integral to a stationary-phase point

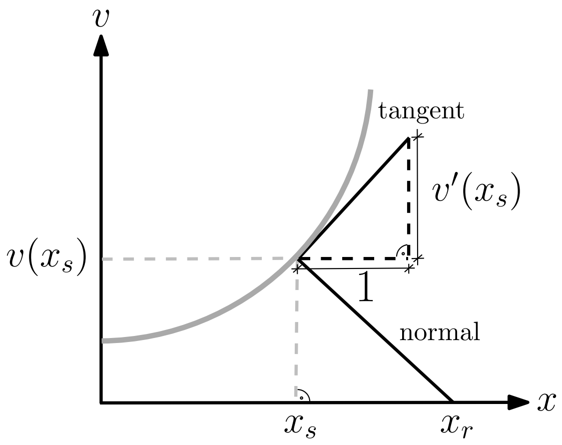

Figure 2.1 – Geometry of tangent and normal at stationary point and its corresponding reference point for a curved source.

$\boldsymbol{x}_s$, which is a point assigned to the point of observation $\boldsymbol{x}_R$. At the point $\boldsymbol{x}_s$ the phase gets maximal, i.e. R gets minimal and $R' = 0$, which coincides with the point of minimum distance.

$$p = \int \frac{e^{-i\,k\,R}}{4\,\pi\,R}\,\sqrt{1+(v')^2}\,\mathrm{d}x \approx \frac{e^{-i\,k\,R}}{4\,\pi\,R}\,\sqrt{\frac{2\,\pi}{k\,R''}}\sqrt{1+(v')^2}\,e^{-i\,\frac{\pi}{4}}\Bigg|_{\boldsymbol{x}_s} \tag{2.5}$$

$$p \approx \frac{e^{-i\left[k\,R+\frac{\pi}{4}\right]}}{\sqrt{8\,\pi\,k}}\,\sqrt{\frac{1+(v')^2}{R^2\,R''}}\Bigg|_{\boldsymbol{x}_s}\,. \tag{2.6}$$

The stationary-phase point is related to the point of observation by

$$\frac{x_r - x_s}{v} = v'\,, \tag{2.7}$$

as derived in appendix A.2 and shown graphically in figure 2.1. Disregarding common factors and the frequency dependency $\frac{1}{\sqrt{k}}$, one would desire that the pressure magnitude becomes independent of the listening position. To this end, the square-root expression has to be constant,

$$c = \frac{R^2\,R''}{1+v'(x)^2}\Bigg|_{\boldsymbol{x}_s}\,. \tag{2.8}$$

By using the derivatives of the distance R and the stationary-phase criterium, shown in Appendix A.2, it turns out that the ideal contour has to be the solution of a second-order non-linear differential equation,

$$c = \frac{v^2\,[1+(v')^2]\,\frac{1+v\,v''+(v')^2}{v\,\sqrt{1+(v')^2}}}{1+(v')^2} \tag{2.9}$$

$$= v\left(\sqrt{1+(v')^2} + \frac{v\,v''}{\sqrt{1+(v')^2}}\right)\,. \tag{2.10}$$

2.2 Numerical Solution

As there is no useful or neat function solving the differential equation (2.10), the solution is rather calculated by numerical methods. For example, MATLAB is able to solve any initial value problem by its implemented ordinary differential equation solvers `ode23` and `ode45`. But there is also the very simple Euler Method to solve the problem with sufficient precision. As it is described in [19], it is assumed that the solution of a differential equation

$$v'(x) = f(x, v) \tag{2.11}$$

can be written as a Taylor series,

$$\begin{align} v(x + \Delta x) &= \sum_k \frac{v^{(k)}|_x}{k!} \Delta x^k \tag{2.12} \\ &= v|_x + \frac{v'|_x}{1!} \Delta x + \frac{v''|_x}{2!} \Delta x^2 + \frac{v'''|_x}{3!} \Delta x^3 + ... \tag{2.13} \end{align}$$

The series is truncated after the first-order term so that

$$v(x + \Delta x) \approx v(x) + \Delta x \, v'(x) \, . \tag{2.14}$$

This means graphically that from a value v at x, the next value $v(x+\Delta x)$ can be found by going along the tangent at $v(x)$ by a sufficiently small step Δx. Assuming a differential equation $v'(x) = f(\Delta x, v(x))$ to be solved, the equation is rewritten by using the discrete step size n. This allows to write the problem finally as a difference equation,

$$v_{n+1} \approx v_n + \Delta x \, f(x_n, v_n) \, . \tag{2.15}$$

To make this usable for the second-order differential equation, a set of first-order differential equations is necessary. Setting $v = \zeta$, $v' = \zeta' = \eta$ and $v'' = g(c, \zeta, \eta)$ yields such a first-order system,

$$\begin{bmatrix} \zeta' \\ \eta' \end{bmatrix} = \begin{bmatrix} \eta \\ c \frac{\sqrt{1+\eta^2}}{\zeta^2} - \frac{1}{\zeta} - \frac{\eta^2}{\zeta} \end{bmatrix} = \begin{bmatrix} \eta \\ g(c, \zeta, \eta) \end{bmatrix} \, . \tag{2.16}$$

For each row, equation (2.15) has to be applied so that the system can be solved numerically by

$$\begin{align} \zeta_{n+1} &= \zeta_n + \Delta x \, \eta_n \tag{2.17} \\ \eta_{n+1} &= \eta_n + \Delta x \, f(\zeta_n, \eta_n) \, . \tag{2.18} \end{align}$$

This solutions allows to build up a simple web-based solver using JavaScript[1]. The relevant excerpt of the JavaScript code is shown in Appendix B. For solving the differential equation numerically, the initial conditions for v and v' are needed. Typically one would

---

[1] `https://lukas_goelles.iem.sh/ocas_web/`

calculate the source for any positions starting at $x = 0$. Therefore $v(0)$ is set as the height of the lowest point of the source. By choosing the nearest point of observation to the array $x_r(0)$, the first derivative at $x = 0$ is fixed by

$$v'(0) = \frac{x_r(0)}{v(0)}, \tag{2.19}$$

following from the stationary-phase condition for R', cf. appendix A.2. Because a value of $c = 1$ will result in a flat curve, i.e. $v(x) =$ const., other values have to be chosen to yield meaningful source contours. Figure 2.2 shows the solution of the differential equation for $c = 2$ with initial conditions $v = 1$ and $v' = 0$. Because the shape of those resulting contours is arched, the source is called Optimally Curved Arc Source (OCAS) in the following. Because the contour can be also seen as a curved line, a synonym for the found term is Optimal Progressively Curved Line Source. As the right plot of figure 2.2 shows the difference between the `ode23` solution of MATLAB and Euler's Method, solving the differential equation using (2.17) and (2.18) is sufficient accurately, as the error in the v axis is always less than $1\,\mathrm{mm}$, so several orders of magnitude below the actual size of the geometry.

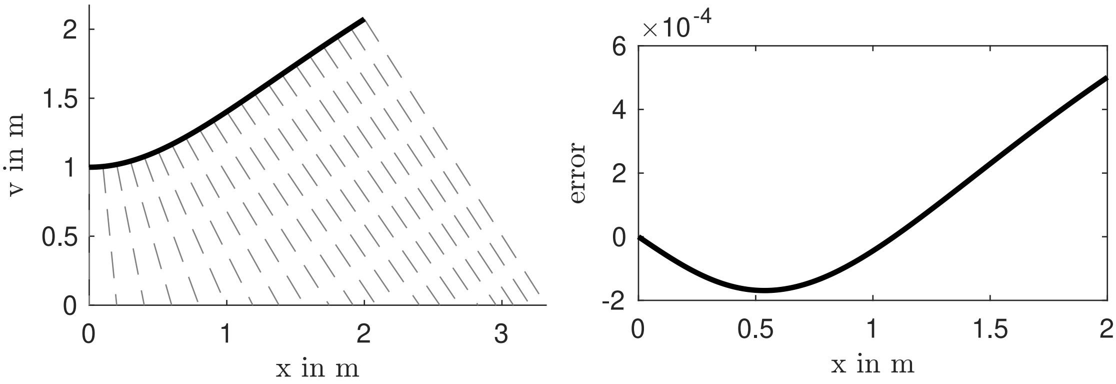

Figure 2.2 – Numerical solution of the differential equation ($c = 2$, initial conditions $v = 1$ and $v' = 0$) with normals connecting the contour with points of observations (left) and numerical error between the `ode23` computation method of MATLAB and solution using the Euler Method by using a step size of $\Delta s = 1\,\mathrm{mm}$ (right).

As also this contour, solved with $c = 2$, will result in a huge source for a large audience area, modifying the value of c will yield more reasonable results. For example the resulting shapes for $c = 10$ and $c = 15$ with the same initial conditions as before are shown in Figure 2.3. As shown in Figure 2.4, a higher value for c will result in higher curvature values. c is therefore the representative parameter for the curvature. Increasing the value of c will therefore yield a steeper contour.

By considering figure 2.4 in detail, it turns out that there are negative values for the curvature which are practically infeasible when using all-positive line-source array splay angles, or when deconstraining the curved source to be convex. Points with $v'' = 0$ are here marked as dotted line. Therefore one is interested in a relationship between the known parameters and the limit at which the curvature changes its sign. Equation (2.18) describes the relation between v, v' and c so that when setting $v'' = 0$ in equation (2.10), we get the following condition,

$$c = v\,\sqrt{1 + v'^2}\,. \tag{2.20}$$

This means that as long $c > v\,\sqrt{1 + (v')^2}$, the curvature stays positive. By considering the limits, until which the solution is valid, see figure 2.3, it turns out that the parameter c determines the farthest point of observation which corresponding point on the contour has positive curvature. Therefore the relationship between v, v', x and x_r from the stationary phase approximation is set into equation 2.20,

$$c = v\,\sqrt{1 + (v')^2} = v\,\sqrt{1 + \frac{(x_r - x)^2}{v^2}} = \sqrt{(x_r - x)^2 + v^2} = R\,. \tag{2.21}$$

It is summarized that the farthest reachable point of observation, for which the curvature of the corresponding point on the contour stays non-negative, is defined by c, and as long as c stays smaller than the distances R between x_r and the source, the curvature is positive.

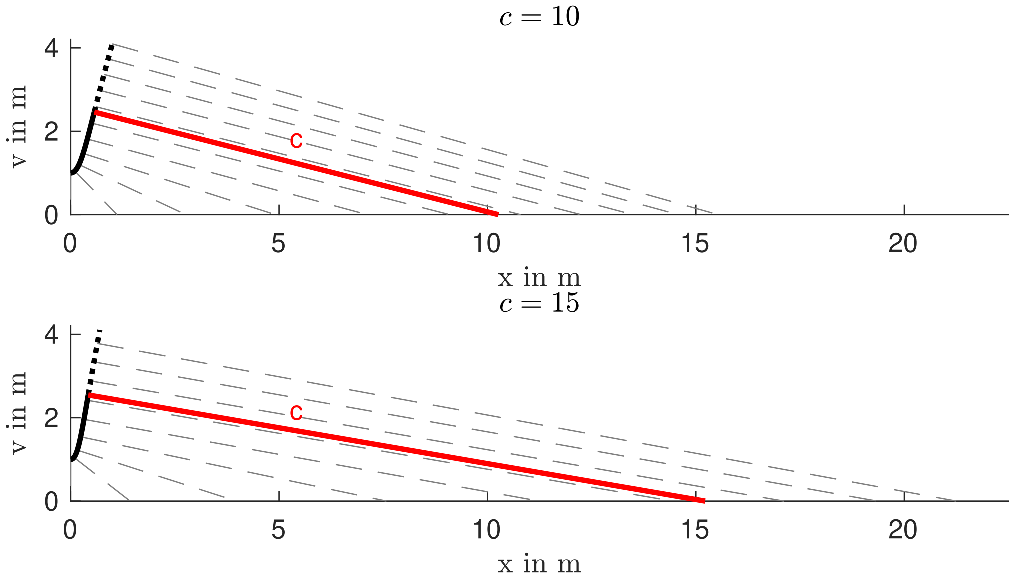

Figure 2.3 – Numerical solutions of the differential equation ($c = 10$ and $c = 15$, initial conditions $v = 1$ and $v' = 0$) with normals connecting the contour with points of observations, dotted lines denote points with $v'' < 0$.

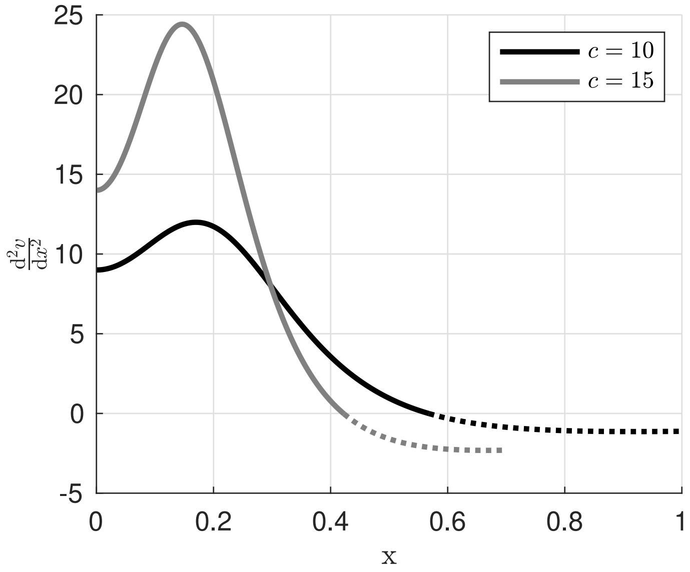

Figure 2.4 – Curvature of the resulting contours shown in Figure 2.3, dotted lines denote $v'' < 0$.

2.3 Waveguide for compact implementations of OCAS

After evaluating the optimal contour for the arc source, one might think that the shape is easy to implement by an array of omnidirectional sources with reasonably narrow spacing, i.e. $\Delta s = 115\,\mathrm{mm}$ (diameter of the compression driver, which is used later). Figure 2.5 simulates the calculated OCAS shape for $c = 15$ with initial conditions $v = 1$ and $v' = 0$ and obviously there is spatial aliasing for high frequencies because the sampling of the contour is too rough. In particular the theoretical spatial aliasing frequency is calculated by

$$f_{\text{aliasing}} = \frac{c}{2\,\Delta s} = \frac{343\,\frac{\mathrm{m}}{\mathrm{s}}}{2 \cdot 0.115\,\mathrm{m}} \approx 1500\,\mathrm{Hz}\,, \tag{2.22}$$

where c denotes the speed of sound ($343\,\frac{\mathrm{m}}{\mathrm{s}}$ at $20\,°\mathrm{C}$) and Δs is the spacing between the sources. Spatial aliasing is expected above a frequency of approximately $1.5\,\mathrm{kHz}$, so at most of the essential operating range of compression drivers, and its results is characterized by position-dependent comb filters in the listening area. But we desire to use the OCAS up to $20\,\mathrm{kHz}$ that requires a maximum distance between the sources of

$$\Delta s = \frac{c}{2\,f_{\text{aliasing}}} = \frac{343\,\frac{\mathrm{m}}{\mathrm{s}}}{2 \cdot 20\,000\,\mathrm{Hz}} = 0.008\,575\,\mathrm{m} = 8.575\,\mathrm{mm}\,. \tag{2.23}$$

As in compact applications it is not economic to deal with multiple small drivers, one would like to use waveguides with a view set of drivers with diameters bigger than $8.575\,\mathrm{mm}$ as continuous arc-shaped source. For line-source arrays as close relatives to the targeted OCAS, multiple solutions for waveguides are found. Two prominent ones

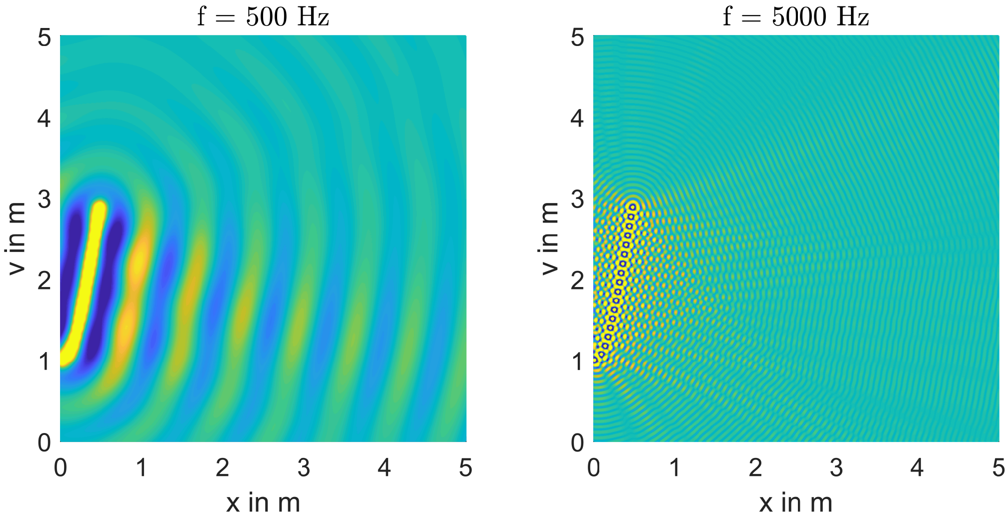

Figure 2.5 – Simulated resulting wavefront for a OCAS at $500\,\mathrm{Hz}$ and $5000\,\mathrm{Hz}$ with multiple point sources at a distance of $115\,\mathrm{mm}$ to each other.

are C. Heil's Diffuseur d'Onde Cylindrique (DOSC, 1992) [8] and E. Vincenot's and F. Deffarge's Hyperbolic Refelctive Wavesource (HRW, 2003) [9]. Both inventions are essential achievements enabling line-source arrays with good directivity behaviour, minimal grating lobes, minimal comb filtering or phasing of neighbouring loudspeaker cabinets in the stack. But for the desired more compact OCAS design, these waveguides typically target a vertically flat or circular output which makes them only useable for large implementation of the OCAS, shown later in section 3.4. We envision a waveguide that allows to vertically shape the wavefront perfectly in the OCAS shape, therefore the isophasic waveguide should precisely assume the particular custom curve resulting as a solution.
To find the paths adaptively the following procedure is proposed to design such a waveguide which orifice is neither vertically flat nor circular.

— **Preparing the OCAS solution**
First the calculated OCAS shape has to be rotated around its lowest point so that the tangent of the highest point of the contour is vertical, its slope is infinity, c.f. Figure 2.6. The v coordinate corresponds here to the z coordinate because the classical cartesian coordinate system is used and the y coordinates of the OCAS are set to 0. The rotation angle is defined as

$$\theta = \frac{\pi}{2} - \arctan\left[v'(x_{\text{max}})\right] , \tag{2.24}$$

where x_{max} denotes the v coordinate of the highest point on the contour. Rotation is done by y rotation basically,

$$\boldsymbol{R}_Y = \begin{bmatrix} \cos\theta & 0 & \sin\theta \\ 0 & 1 & 0 \\ -\sin\theta & 0 & \cos\theta \end{bmatrix} . \tag{2.25}$$

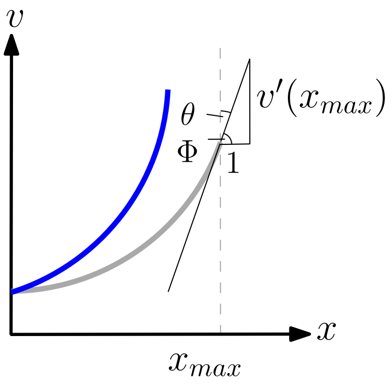

Figure 2.6 – Original OCAS contour (grey) with tangent and angles to calculated the rotated contour (blue).

As we want to start with a cone at the compression driver side, a cone of height h_c and radius r_c is needed, which circular base is defined as

$$\boldsymbol{x}_C = \begin{bmatrix} h_c \\ r_c \sin\varphi \\ r_c \cos\varphi \end{bmatrix} \qquad \text{with } \varphi \in [0, 2\pi)\,. \tag{2.26}$$

Now every point of the circle has to be connected with the contour, which later represents the orifice, as shown for a few points in figure 2.7. Discretizing at a uniform angle should thereby correspond to a uniform discretization of the natural length parameter s of the contour.

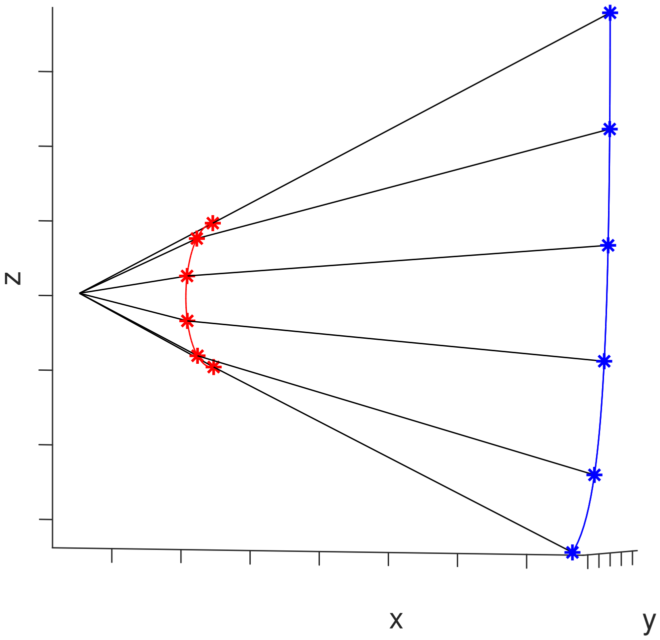

Figure 2.7 – First step: Waveguide starting with a cone connecting a few points of the circular base with the corresponding points on the OCAS contour.

- **Vertical Adaptation**
  With all paths projected onto the xz plane polynomials are designed that should fulfill the following properties:
  - The polynomial ends perpendicular to the tangent at the orifice, which is implied by the stationary phase method.
  - The degree of the polynomial is 3.
  - Start and end endpoint of the polynomial is fixed by the orifice (OCAS shape) and the circular base of the cone.
  - The tangent at the circular base of the cone must correspond to its slope to guarantee a smooth transition.

  For an arbitrary orifice contour, which is neither a line nor a circle with centre on the x axis, we find that the path length of the polynomial for $\varphi = 0$ and for $\varphi = \pi$ are unequal. But equal path lengths are required for these two extreme angles because they are not altered by projection onto the xy plane. The cone is shifted in z direction to equalize the path lengths for $\varphi = 0$ and $\varphi = \pi$ before the preliminary polynomials of all other angles are calculated. This resulting path length is final and becomes the target length at all other angles. Figure 2.8 shows the adapted vertical paths for $\varphi = 0$ and $\varphi = \pi$ after z shift. The length of a polynomial $p(x)$ can be calculated by solving

$$L = \int_{x_1}^{x_2} \sqrt{1 + p'(x)^2}\,\mathrm{d}x\,. \tag{2.27}$$

  This integral is not easily solved analytically for the resulting polynomials so that their lengths are calculated numerically. The Matlab function `arclength` turned out to be helpful in doing so [20].

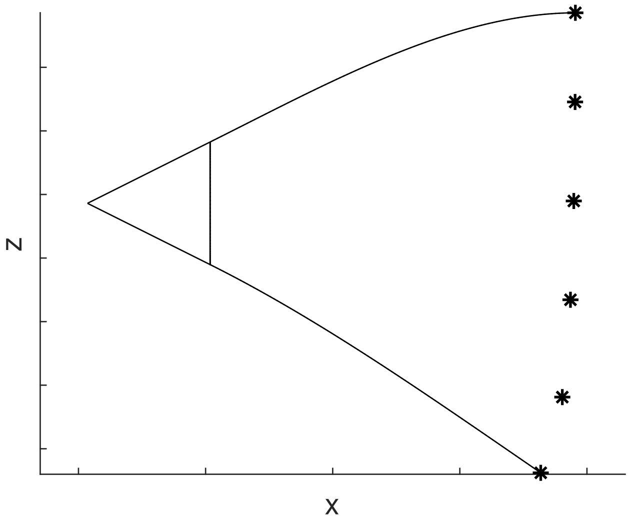

Figure 2.8 – Adapted paths for $\varphi = 0$ and $\varphi = \pi$ after z shift with small cone at the beginning.

- **Horizontal Adaptation**
  After calculating the vertical polynomials for the angles $0 < \varphi < \pi$, these polynomials have to be bent horizontally so that all path lengths are equal. For this

purpose, we consider a plane on which 2D polynomials are designed. For a plane to be fully defined, 3 points are required at least. As we already know 2 of it, i.e. the point on the circular base of the cone and the point on the orifice, the missing one is brought by setting a second larger cone that is proportional to the one we already have,

$$\boldsymbol{x}_{C,2} = \begin{bmatrix} h_{c,2} \\ r_{c,2}\,\sin\varphi \\ r_{c,2}\,\cos\varphi \end{bmatrix} \qquad \text{with } \varphi \in [0, 2\pi) \tag{2.28}$$

$$\frac{h_{c,2}}{h_c} = \frac{r_{c,2}}{r_c} \implies r_{c,2} = \frac{h_{c,2}}{h_c}\, r_c\,. \tag{2.29}$$

The plane is defined by its normal vector calculated by the point of the first cone $\boldsymbol{x}_c$, the point of the second cone $\boldsymbol{x}_{c,2}$ and the corresponding point on the orifice $\boldsymbol{x}_o$,

$$\boldsymbol{n}_{\text{Plane}} = \begin{bmatrix} x_n \\ y_n \\ z_n \end{bmatrix} = \left(\boldsymbol{x}_{c,2} - \boldsymbol{x}_c\right) \times \left(\boldsymbol{x}_{c,2} - \boldsymbol{x}_o\right)\,, \tag{2.30}$$

and its shift on the z axis is calculated by inserting $\boldsymbol{x}_c$

$$d = -x_n \cdot h_c - y_n \cdot r_c \cdot \sin\varphi + r_c \cdot \cos\varphi\,. \tag{2.31}$$

The plane is described by

$$x_n \cdot x + y_n \cdot y + z_n \cdot z + d = 0 \tag{2.32}$$

to correspond with its standard form. To design 2D polynomials in MATLAB this plane must correspond with the xy plane. Therefore a z shift by $-\frac{d}{n_z}$ followed by a rotation around the axis spanned by $\boldsymbol{u} = \begin{bmatrix} \frac{n_y}{\sqrt{n_x^2+n_y^2}} & \frac{-n_x}{\sqrt{n_x^2+n_y^2}} \end{bmatrix}^T = \begin{bmatrix} u_x & u_y & 0 \end{bmatrix}^T$ around Θ is done. The rotation angle Θ is calculated as the angle between the normal of the plane and the normal of the xy plane, i.e.

$$\Theta = \arccos\left(\begin{bmatrix} 0 & 0 & 1 \end{bmatrix} \cdot \frac{\boldsymbol{n}_{\text{Plane}}}{\|\boldsymbol{n}_{\text{Plane}}\|}\right)\,. \tag{2.33}$$

By applying the rotation matrix, cf. appendix A.5

$$\boldsymbol{R}_U = \begin{bmatrix} \cos\Theta + u_x^2\,(1-\cos\Theta) & u_x\,u_y\,(1-\cos\Theta) & u_y\,\sin\Theta \\ u_x\,u_y\,(1-\cos\Theta) & \cos\Theta + u_y^2\,(1-\cos\Theta) & -u_x\sin\Theta \\ -u_y\,\sin\Theta & u_x\,\sin\Theta & \cos\Theta \end{bmatrix}\,, \tag{2.34}$$

the rotated points $\boldsymbol{x}_{R,c}$, $\boldsymbol{x}_{R,c2}$, $\boldsymbol{x}_{R,o}$ are used as control points in the polynomial design in the next step.

In the rotated plane, the horizontal polynomials are designed with the following properties:

— The degree of the polynomials is 4.

— $\boldsymbol{x}_{R,c}$, $\boldsymbol{x}_{R,c2}$, $\boldsymbol{x}_{R,o}$ have to be points on the polynomial.
— The tangent at $\boldsymbol{x}_{R,c}$ must correspond to the slope of the cone to guarantee smooth transition.

After the design process, the polynomial has to be rotated and shifted so that all three supporting points result in their original position. Now the z coordinate of the resulting polynomial is replaced by the z coordinate calculated in the vertical adaptation process. This step corresponds to modifying the plane to a curved surface with postulated properties mentioned above. Now the path length has to be considered. If the difference to the target path length is out of tolerance (e.g. $3\,\mathrm{mm}$), the adaptation has to be redone by moving $\boldsymbol{x}_{r,c,2}$ into the y direction whenever the path length is too short or negatively otherwise.

Figure 2.9 shows the four basic steps to do the horizontal adaptation. As the waveguide has to be mirror-symmetrical to the y axis, the adaptation process can be done for $\varphi \in [0, \pi]$ only and then be complemented to the negative y axis by mirroring.

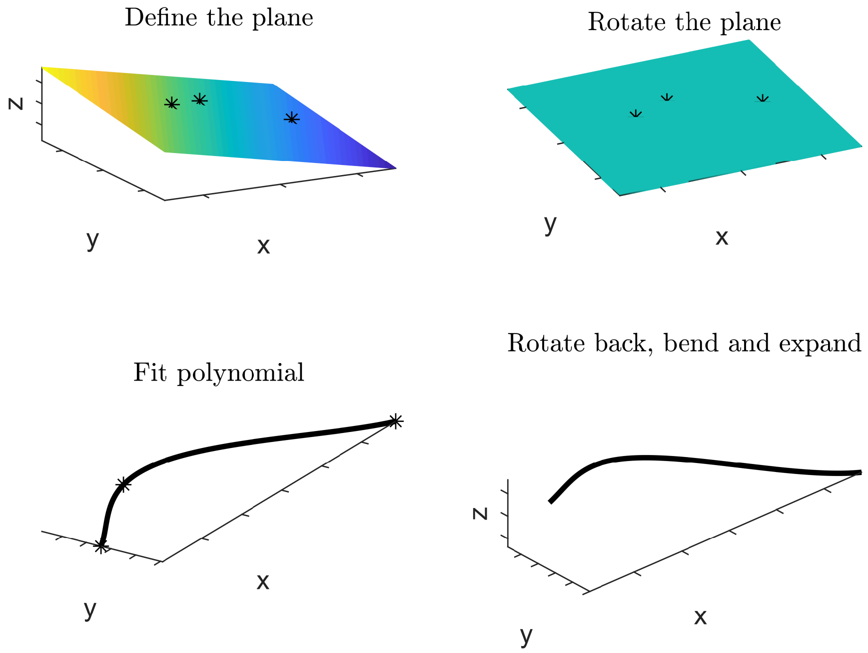

Figure 2.9 – Basic steps of the horizontal adaptation process.

A graphical representation of three essential steps, horizontal and vertical polynomial design before and after the path length adaptation, is shown in figure 2.11. After this procedure one would receive a body similar to the one shown in figure 2.10. The compression driver at its apex would drive waves along two of its parallel, convex shells. To export any body or shell design out of MATLAB to import it later in any CAD software or in the slicer of the 3D printer, using the function `surf2stl` [21] was quite helpful.

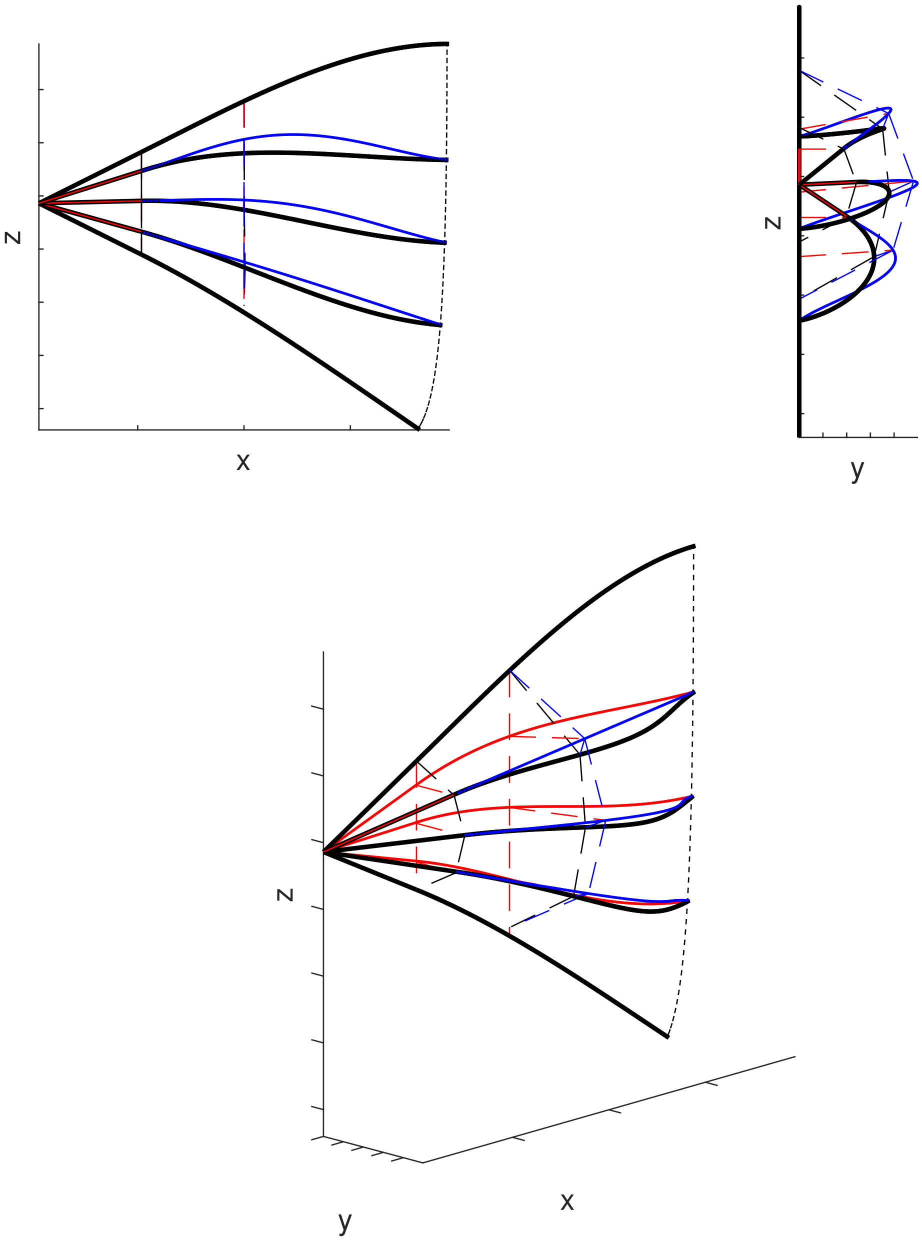

Figure 2.10 – Steps of the purposed procedure: 1. vertical polynomial design (red), 2. horizontal polynomial design with second cone (blue) 3. modified version of the horizontal polynomial for equal path length (black).

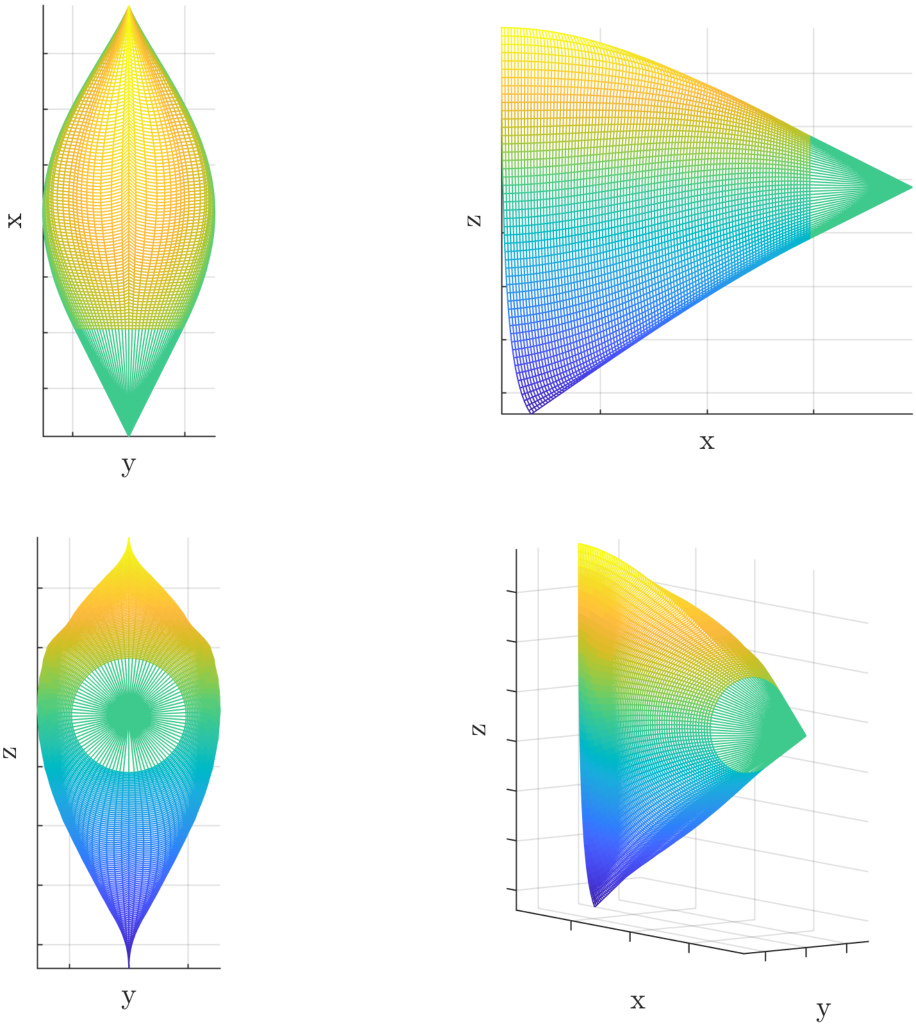

Figure 2.11 – Different views of the interior body of the waveguide.

2.4 Axissymmetric surface source that would additionally cover the azimuth evenly with direct sound

As the design is not fixed for curves in x and v that resulted in the one-dimensional integral of the Green's function of the previous chapters, one would also consider an optimally curved surface in the three-dimensional space. We think of an axisymmetric surface in 3D, i.e. one that consists of a rotated curve that is originally designed in the xv plane and then rotated around v to get an axisymmetric shape. Frenet-Seret formulas are used to describe a one-dimensional curve in three dimensions. Any such curve is defined on its natural length coordinate s and its cartesian position vector $\boldsymbol{r}$ for every position on the curve. The derivative of the curve yields the unit-length tangential vector $\boldsymbol{t}$,

$$\frac{\mathrm{d}\boldsymbol{r}}{\mathrm{d}s} = \boldsymbol{t}, \qquad \|\boldsymbol{t}\| = \left\|\frac{\mathrm{d}\boldsymbol{r}}{\mathrm{d}s}\right\| = \lim_{\Delta s\to 0} \frac{\|\boldsymbol{r}(s+\Delta s) - \boldsymbol{r}(s)\|}{\Delta s} = \frac{\Delta s}{\Delta s} = 1\,. \tag{2.35}$$

The derivative of the unit-length tangential vector yields a curvature-proportional version of the unit-length normal vector $\boldsymbol{n}$ that points towards the center of a circle with radius ρ. This radius is reciprocal to the curvature κ of the curve, i.e. $\kappa = \frac{1}{\rho}$,

$$\rho\,\frac{\mathrm{d}\boldsymbol{t}}{\mathrm{d}s} = \boldsymbol{n}, \qquad \left\|\frac{\mathrm{d}\boldsymbol{t}}{\mathrm{d}s}\right\| = \lim_{\Delta s\to 0} \frac{\|\boldsymbol{t}(s+\Delta s) - \boldsymbol{t}(s)\|}{\Delta s} = \frac{1}{\rho}\,\frac{\mathrm{d}\varphi}{\mathrm{d}\varphi} = \kappa\,. \tag{2.36}$$

The third coordinate is assumed to come from rotation of the curve $\boldsymbol{r}$ around the z axis with the variable polar angle φ,

$$\boldsymbol{r} = \begin{bmatrix} x(s)\,\cos(\varphi) \\ x(s)\,\sin(\varphi) \\ v(s) \end{bmatrix}\,. \tag{2.37}$$

The coordinates of the points of observation are $\boldsymbol{x}_R = \begin{bmatrix} x_r & 0 & 0 \end{bmatrix}^T$ so that the distance R yields

$$R = \|\boldsymbol{x}_r - \boldsymbol{r}\| = \sqrt{x_r^2 + x(s)^2 - 2\,x(s)\,x_r\,\cos(\varphi) + v(s)^2}\,. \tag{2.38}$$

This distances appears again in the oscillating integrand but with conical surface integration constants $x(s)\,\mathrm{d}\varphi\,\mathrm{d}s$,

$$p = \iint \frac{e^{-i\,k\,R}}{4\,\pi\,R}\,x(s)\,\mathrm{d}\varphi\,\mathrm{d}s\,. \tag{2.39}$$

As in the chapter about OCAS, the value of the integral is approximated by the stationary phase method using the distance $R = R_s$ at which the derivatives of R with respect to s and φ vanish. As the coordinates s and φ are orthogonal by definition, the Hessian is diagonal whose determinant is required in the square root. We get for the approximated integral,

$$p \approx \frac{e^{-i\,k\,R_s}}{4\,\pi\,R_s}\,\frac{2\,\pi\,x_s}{-i\,k\sqrt{\frac{\mathrm{d}^2 R_s}{\mathrm{d}s^2}\,\frac{\mathrm{d}^2 R_s}{\mathrm{d}\varphi^2}}}\,. \tag{2.40}$$

With the second derivatives of appendix A.3 inserted, the approximated integral becomes

$$p_{2D} \approx \frac{e^{-i\,k\,R_s}}{4\,\pi\,R_s}\,\frac{1}{\sqrt{\frac{x_r}{x}}\,\left(1+\kappa\,R_s\right)}\,. \tag{2.41}$$

Alternatively performing the integral only over $\mathrm{d}s$, as one-dimensional integral, yields

$$p_{1D} \approx \frac{e^{-i\,k\,R_s}}{\sqrt{-i\,8\,\pi\,k}}\,\frac{1}{\sqrt{R_s\,\left(1+\kappa\,R_s\right)}}\,. \tag{2.42}$$

To assemble the differential equations, the curvature κ has to be related to the know parameters. With appendix A.4 and the relation of R_s and v from the previous section, $R_s = v\,\sqrt{1+(v')^2}$, the integrals for both numbers of surface dimensions becomes,

$$p_{1D} \approx \frac{e^{-i\,k\,R_s}}{\sqrt{-i\,8\,\pi\,k}}\,\frac{1}{\sqrt{v\,\left(\sqrt{1+(v')^2}+\frac{v\,v''}{\sqrt{1+(v')^2}}\right)}} \tag{2.43}$$

$$p_{2D} \approx \frac{e^{-i\,k\,R_s}}{-i\,2\,k}\,\frac{1}{\left(1+\frac{v\,v'}{x}\right)\,\left(1+\frac{v\,v''}{1+(v')^2}\right)}\,. \tag{2.44}$$

As before, the sound pressure level is desired to be be independent of the listener position, which yields the differential equation for 1D that we already know from above

$$v\,\left(\sqrt{1+v'^2}+\frac{v\,v''}{\sqrt{1+v'^2}}\right) = c\,, \tag{2.45}$$

and as 2D axisymmetric shape around z, we get the differential equation for the generating curve in xz (with $v = z$)

$$\left(1+\frac{v\,v'}{x}\right)\,\left(1+\frac{v\,v''}{1+v'^2}\right) = c\,. \tag{2.46}$$

Again we are interested in the point at which $v'' = 0$,

$$c = 1+\frac{v\,v'}{x} = 1+\frac{x+x_r}{x} = \frac{x_r}{x}\,. \tag{2.47}$$

This condition is useful, as it means that the farthest possible point of observation is defined as the c multiple of the x coordinate of $v'' = 0$, i.e. $x_r = c\,x$. Note the contrast to the meaning of c in chapter 2.1 that defined a maximum distance between the source and receiver in the 1D case. The 2D differential equation is also solved by Euler's Method. After evaluating the differential equation, the positions in space have to be calculated as mentioned in equation (2.37) by rotating around the z axis. As an example, the solutions for $c = 30$ with initial conditions $v = 1$ and $v' = 0$ are plotted in figure 2.12 where the audience area is defined as the xy plane. Figure 2.13 shows the upper-bound contour so that a rectangular listening area of $30\,\mathrm{m} \times 30\,\mathrm{m}$ is covered. As the aim of this thesis is to build a curved one-dimensional source and to compare it to the existing source types, the surface source is left as a basic example that might be interesting for future work.

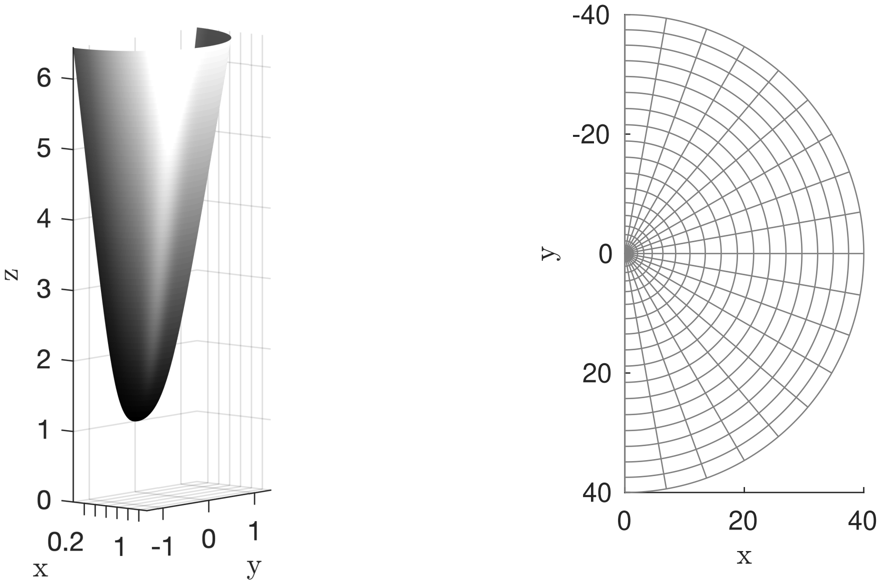

Figure 2.12 – Solution of the 2D differential equation for $c = 30$ (left) and resulting grid of points of observations (right).

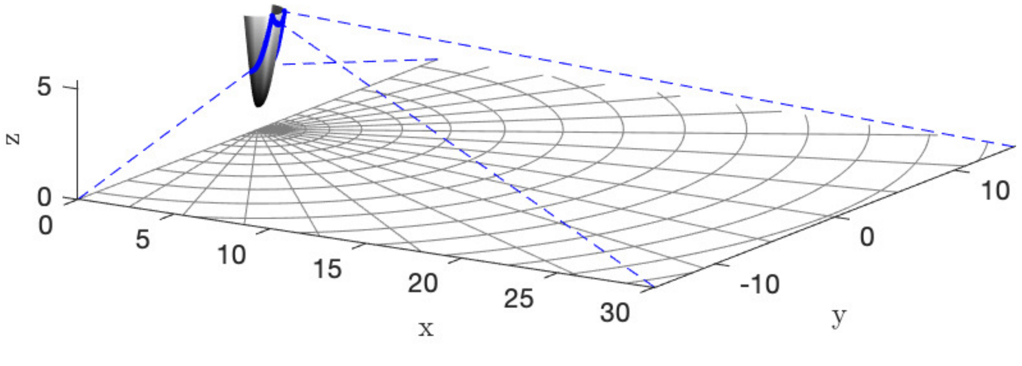

Figure 2.13 – Surface source with upper-bound contour to cover an audience area of $30\,\mathrm{m} \times 30\,\mathrm{m}$.

Chapter 3

Simulations

This chapter discusses numerical simulations of different OCAS configurations. For simplicity they show the superposition of multiple ideal point sources (except simulations done by Soundvision). The frequency dependency of the stationary phase approximated integral is compensated by a pink filter ($3\,\mathrm{dB}$ per octave, $\sqrt{k}$). To make those simulations comparable to software tools provided by the known loudspeaker manufacturing companies (L'Acoustics, Nexo, d&b, Meyer, ...), the frequency response over the listening plane is also shown with averaging in third-octave bands or as A-weighted wideband responses. The used A-filter is described mathematically in [22] and shown in Figure 3.1,

$$A(f) = 20\,\lg\left[\frac{f_4^2\,f^4}{(f^2+f_1^2)\,\sqrt{f^2+f_2^2}\,\sqrt{f^2+f_3^2}\,(f+f_4)^2}\right] - A_{1000}\,, \tag{3.1}$$

with $f_1 = 20.6\,\mathrm{Hz}$, $f_2 = 107.7\,\mathrm{Hz}$, $f_3 = 737.9\,\mathrm{Hz}$, $f_4 = 12\,194\,\mathrm{Hz}$ and $A_{1000} = 2\,\mathrm{dB}$.

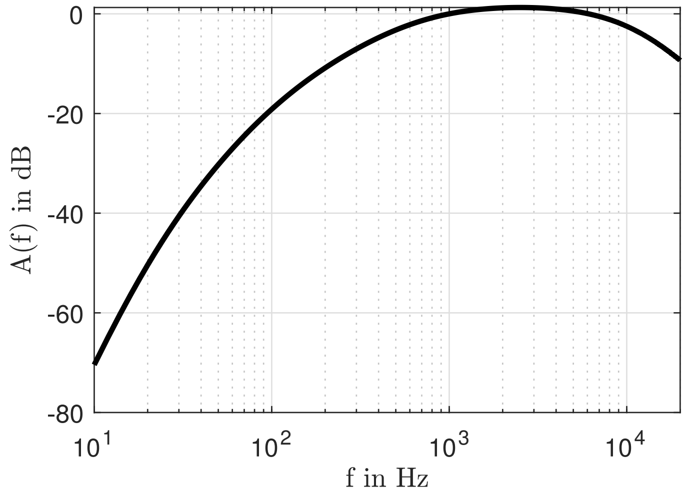

Figure 3.1 – A-weighting filter from Equation (3.1) that is used to display wideband results of the simulations

3.1 Simulations showing coverage behaviour

As a first simulation, an OCAS is considered with curvature/distance parameter set to $c = 15$ and initial conditions $v = 1$ and $v' = 0$. Figure 3.2 shows the contour of the corresponding OCAS as well as its normals connecting the points of observation with the contour. This OCAS reaches its farthest point of observation at approximately $10.5\,\mathrm{m}$. The source is cut before the point with $v'' = 0$ is reached. The bottom of figure 3.2 moreover shows the frequency response over the audience area for the OCAS compared to a single point source. The supported audience area is now defined as the area in which the direct-sound level stays above $-6\,\mathrm{dB}$. This source meets the design criteria above $1\,\mathrm{kHz}$ for the audience area designed with the parameter $c = 15$.

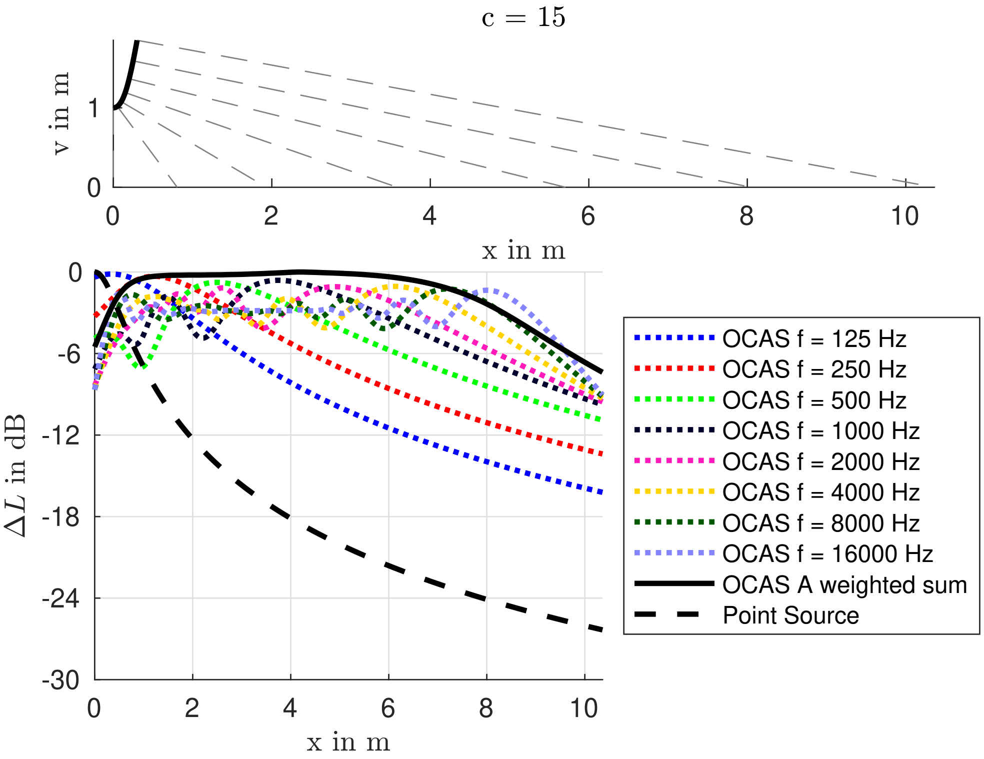

Figure 3.2 – Contour with normals connecting the points of observation with the contour (top) and simulation of the direct-sound level for different frequencies with A-weighted sum compared to the sound level of a single point source (bottom).

Considering the A-weighted sum, the loudness within most of the audience area is expected to be equal. Close to the source there is a roll-off, as well as at the end of the audience area. This is caused by boundary effects because the stationary phase approximation assumes integral boundaries from $-\infty$ to ∞ which is not supported by the real finite source. Close to the source this effect does not matter much because the attenuation at $x_r = 27\,\mathrm{cm}$ is $3\,\mathrm{dB}$ compared to the loudest point of observation, at $x_R = 1\,\mathrm{m}$ it is $0.45\,\mathrm{dB}$. But for more distant points of observation, this roll-off plays an essential role. For $x_R = 8.3\,\mathrm{m}$, there is already an attenuation of $3\,\mathrm{dB}$, at $x_R = 9.7\,\mathrm{m}$ it is $6\,\mathrm{dB}$. If the $6\,\mathrm{dB}$ criterion is considered for the A-weighted sum, the limit is reached at a point of observation of $10\,\mathrm{m}$ so that the A-weighted coverage reaches nearly the entire target distance.

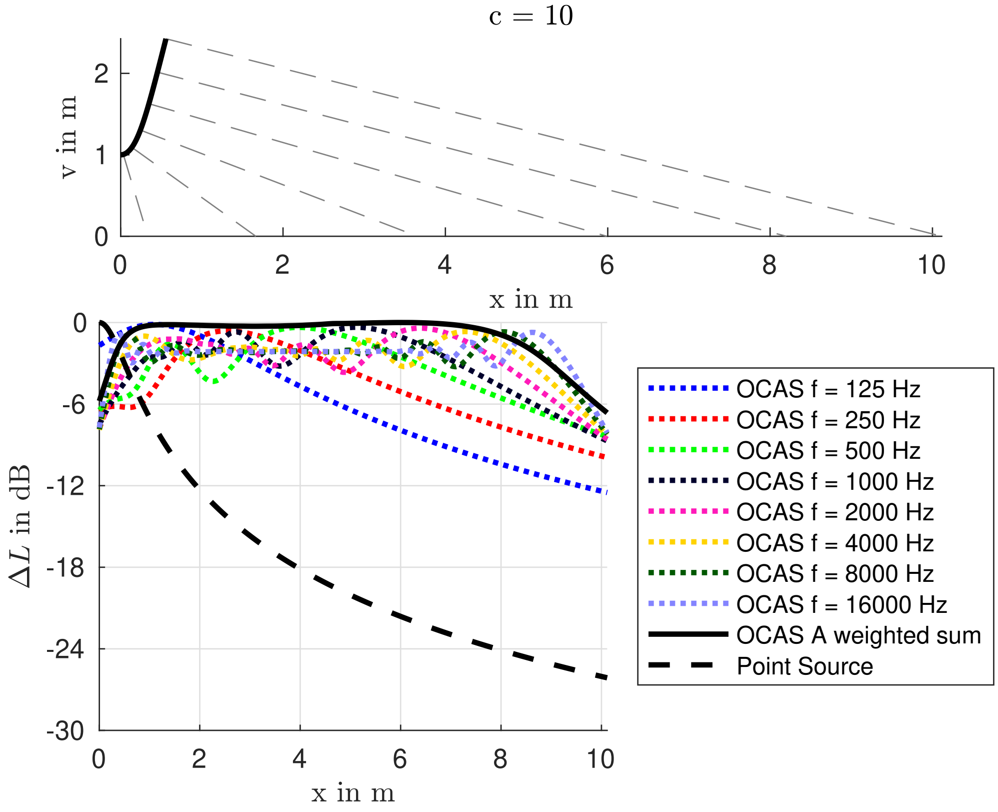

Figure 3.3 – Contour with normals connecting the points of observation with the contour (top) and simulation of the direct-sound level for different frequencies with A-weighted sum compared to the sound level of a single point source (bottom).

To reach a constant sound pressure for lower frequencies, the OCAS has to be larger. A larger source covering the same means to decrease the curvature parameter c, for example it is reduced to $c = 10$. In this case the height of the source is exploit best because at the highest point $v''(x)$ is nearly 0. Figure 3.3 shows that the $6\,\mathrm{dB}$ condition for the audience area is now met for frequencies above $500\,\mathrm{Hz}$. Compared to the results before, this setting also improves the A-weighted sum so that a bigger part of the audience is provided with (nearly) equal loudness. For the area very close to the source it does not matter, but for $x_r = 9\,\mathrm{m}$, there is an attenuation of $3\,\mathrm{dB}$ while for $x_r = 9.9\,\mathrm{m}$ it is $6\,\mathrm{dB}$. This means that increasing the size will yield a flatter A-weighted coverage, but also a steeper roll-off on the further end of the listening area. But on the other hand, one should not forget that the new OCAS is 1.7 times bigger than before. So there is a trade-off between flat coverage for a wide frequency range together with a wider A-weighted flat coverage and the size.

The radiation behaviour is another interesting aspect to consider if the condition that the source has to be convex, i.e. $v''(x) \geq 0$, is ignored. Figure 3.4 shows that for farther points of observation, the source has a focusing impact. Interestingly in this case, the postulated flatness is improved further, also at low frequencies.

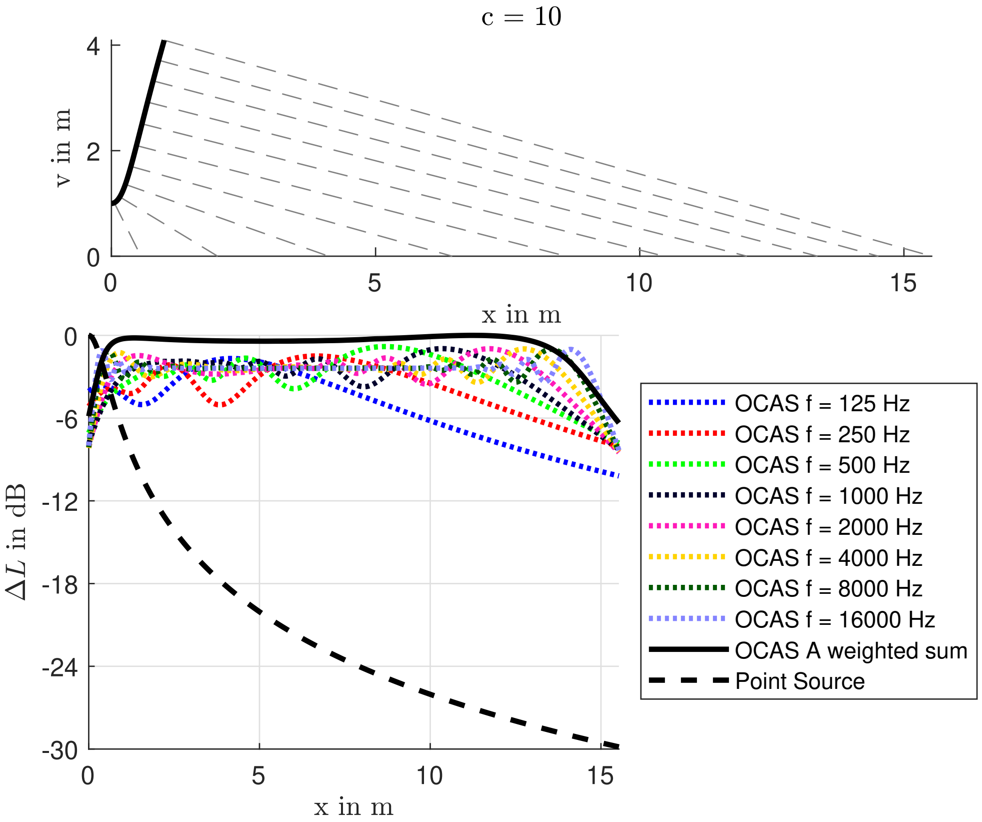

Figure 3.4 – Non-convex OCAS that extends beyond $v'' = 0$.

To avoid negative curvatures by simultaneously increasing the OCAS size to see the impact on lower frequencies, one could continue with constant tangent slope beginning at $v''(x) = 0$. Figure 3.5 shows the resulting shape as well as the frequency dependent coverage. In general continuing with constant tangent slope will not yield drastic changes. On closer inspection it turns out that this solution will influence the amplitude for farther points of observation. Nevertheless the position at which the $-6\,\mathrm{dB}$ line is cut by the graph of the A-weighted sum does not differ substantially compared to the exact solution because the difference in the v coordinate between the exact solution and the solution with constant tangent is always less than $4\,\mathrm{cm}$ in all cases.

Therefore it should be noted that instead of trying to build a source that focuses farther points of observation, following a shape where the tangent slope stays constant starting at $v''(x) = 0$ has to be preferred.

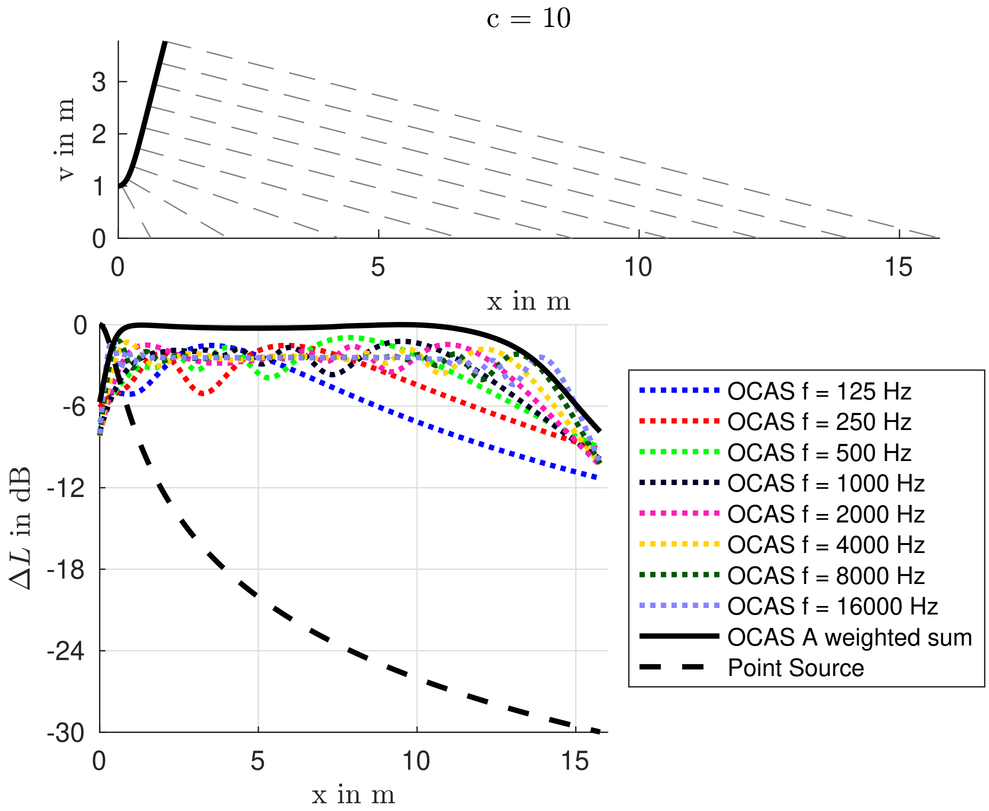

Figure 3.5 – OCAS with continued constant tangent slope from $v'' = 0$.

3.2 Near field - far field

As shown before for different OCAS sizes covering the same audience area, it turns out that the arc length of the source is related to the lower frequency at which the $6\,\mathrm{dB}$ condition is not met anymore. In a simple approximation assuming that the source is not extended much in x direction, the arc length may be replaced by the source height h. In particular, doubling the height will reduce this frequency by a quarter, cf. figure 3.6.

As it is done in [4] for line sources, also for the OCAS the transition radius between near and far field is calculated by observing the distance between nearest and farthest point on the contour for a point of observation x_r

$$d = \sqrt{(x_r - x_e)^2 + v_e^2} - \sqrt{x_r^2 + v_0^2}\,, \tag{3.2}$$

where x_0/v_0 denotes the x/v coordinate of the lowest point of the contour and x_e/v_e the x/v coordinate of the highest point of the contour. Because it is assumed that x_e is small in comparison to the size of the audience area, i.e. $x_e \ll x_{r,max}$, $x_r - x_e \approx x$. The distance is therefore approximated by $d \approx \sqrt{x_r^2 + v_e^2} - \sqrt{x^2 + v_0^2}$. If the phase difference

$$\Phi = k\left[\sqrt{x_r^2 + v_e^2} - \sqrt{x_r^2 + v_0^2}\right] \tag{3.3}$$

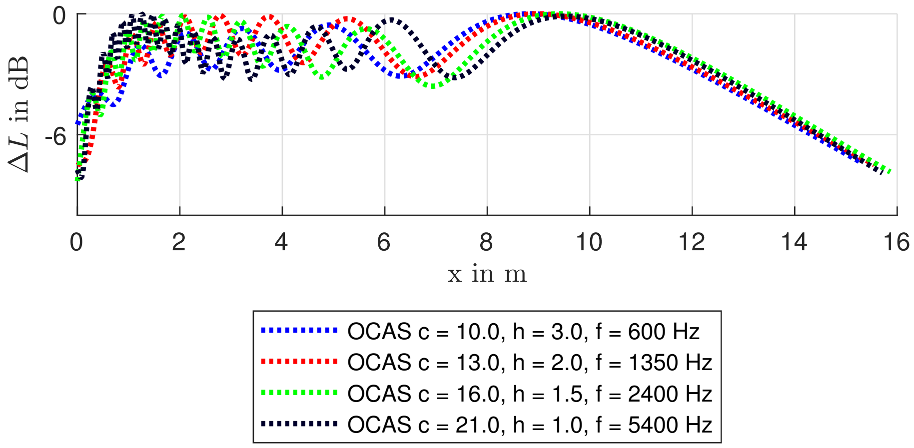

Figure 3.6 – Simulation of the direct-sound level for different OCAS settings for different frequency showing the inverse relationship between the height and the critical frequency.

$$= k\, x_r \left[\sqrt{1 + \frac{v_e^2}{x_r^2}} - \sqrt{1 + \frac{v_0^2}{x_r^2}} \right] \tag{3.4}$$

$$\approx k\, x_r \left[\frac{1}{2} \frac{v_e^2}{x_r^2} - \frac{1}{2} \frac{v_0^2}{x_r^2} \right] = \frac{1}{2}\, k\, \frac{(v_e - v_0)^2}{x_r} = \frac{k\, h^2}{2 x_r} \leq \frac{\pi}{2} \tag{3.5}$$

(using the binomial approximation $(1 + x)^\alpha \approx 1 + \alpha\, x$) stays limited by $\frac{\pi}{2}$, the distance for the transition from near to far field becomes

$$x_r = \frac{k}{\pi}\, h^2 = \frac{2\pi\, f}{\pi\, c}\, h^2 = \frac{2\, f\, h^2}{c}\, . \tag{3.6}$$

This result is very similar to the near/far field transition radius of a line source of length L,

$$r = \frac{f\, L^2}{2\, c}\, . \tag{3.7}$$

Comparing the near/far field radius for the OCAS and a line source, there is a factor 4 in between. This factor comes from the observation of a finite line source which is expanded along the v axis from $-\frac{L}{2}$ to $\frac{L}{2}$ so that the distance is calculated by the half of the source length while for the OCAS rather the whole length appears to be relevant.

Figure 3.7 shows this equation graphically for different source sizes as a function of the frequency f. As a sanity check, the OCAS of Figure 3.2 is considered. It was mentioned that for this source height of approximately $1\,\mathrm{m}$ for a distance of $10\,\mathrm{m}$ to be covered, the usable frequency range is limited by the lower frequency of $1000\,\mathrm{Hz}$. The formula and the figure indicates a near to far field critical frequency of

$$f = \frac{343 \cdot 10}{2 \cdot 1^2} = 1715\,\mathrm{Hz}\, , \tag{3.8}$$

by considering a fixed distance of $10\,\mathrm{m}$. And also the simulation of Figure 3.3 (OCAS height: $1.7\,\mathrm{m}$) claims a frequency of

$$f = \frac{343 \cdot 10}{2 \cdot 1.7^2} = 593.43\,\mathrm{Hz}\,. \tag{3.9}$$

This calculation coincides with the estimations done by the octave band simulation so that the chart and the formula provide a simple a prior assessment of the frequency dependent covered area.

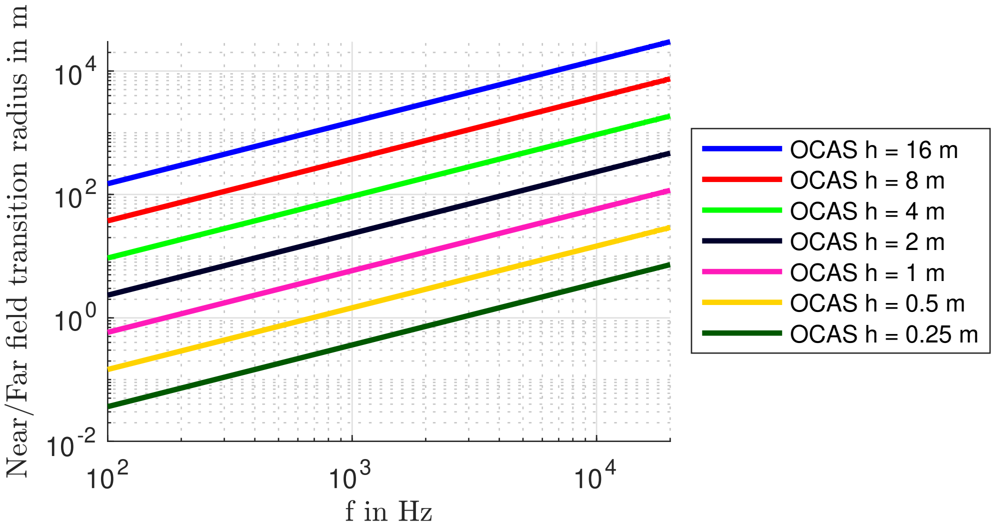

Figure 3.7 – Near/Far field transition radius as a function of the frequency.

3.3 Misconfiguration

The previous discussions gave some insight of the OCAS coverage behaviour. This observations are only valid in practise if the source is set up correctly. Therefore it is also interesting whether the source is not positioned optimally, i.e. a different vertical distance between the lowest point of the source and the audience v_0, i.e. $v(0) \neq v_0$ is chosen or the first point of observation is shifted by rotation.

Again the OCAS from figures 2.3 and 3.2 is considered. In these figures, $v(0)$ was set to 1. Now the source is shifted in v direction by $1\,\mathrm{m}$, so that $v_0 = 2$ although the shape was calculated for $v(0) = 1$. Figure 3.8 shows the contour and the normals connecting the source with the points of observations. Comparing to the correct setup, it seems that a wider area is covered. The source in correct setup should cover up to $10\,\mathrm{m}$ while this simulation shows a farthest point of observation of $25.8\,\mathrm{m}$. But as the figure shows, the postulated flatness is disturbed. Not only the curve of the A-weighted sum but also for some high frequencies, one observes for the misaligned source boosted levels for points of observation between $8\,\mathrm{m}$ and $12\,\mathrm{m}$ when compared to points closer to the source. There is a loudness difference of $2\,\mathrm{dB}$ between $x_r = 1.3\,\mathrm{m}$ and the loudest point that lies at $9.14\,\mathrm{m}$.

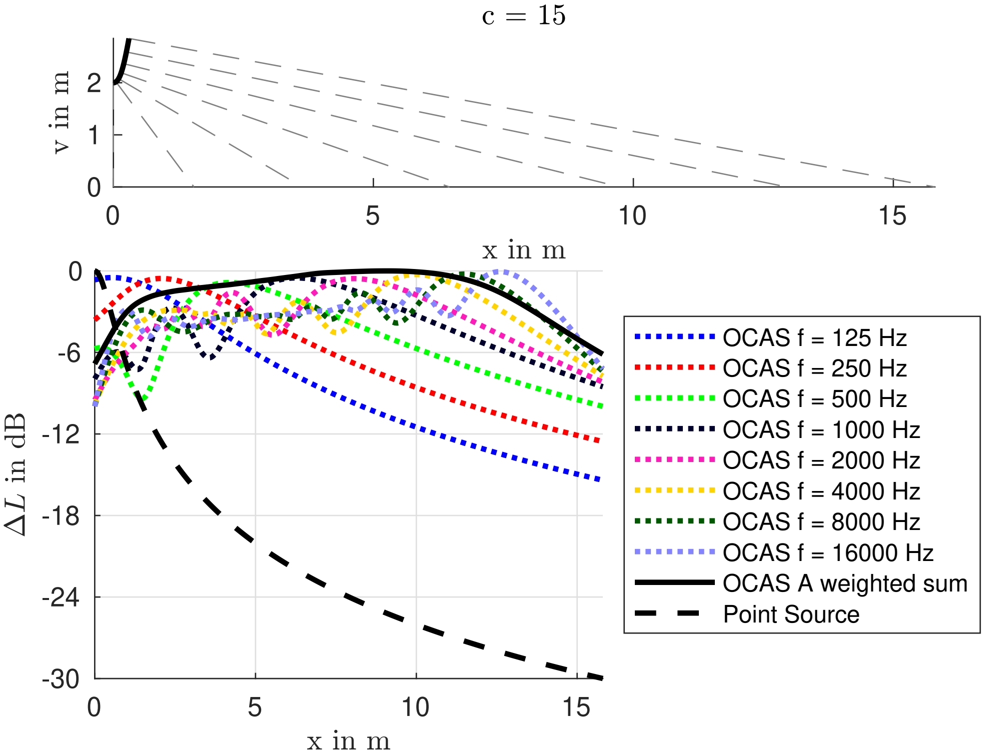

Figure 3.8 – OCAS contour with normals connecting the source with the points of observation calculated with $v(0) = 1$, but positioned at $v_0 = 2$ (top) and coverage behaviour for different frequencies as well as A-weighted sum (bottom).

A less drastic vertical displacement ($v_0 = 1.25$) is shown in figure 3.9. For example, at $x_r = 9.9\,\mathrm{m}$ the attenuation of the original correct set up version was $6\,\mathrm{dB}$ while in

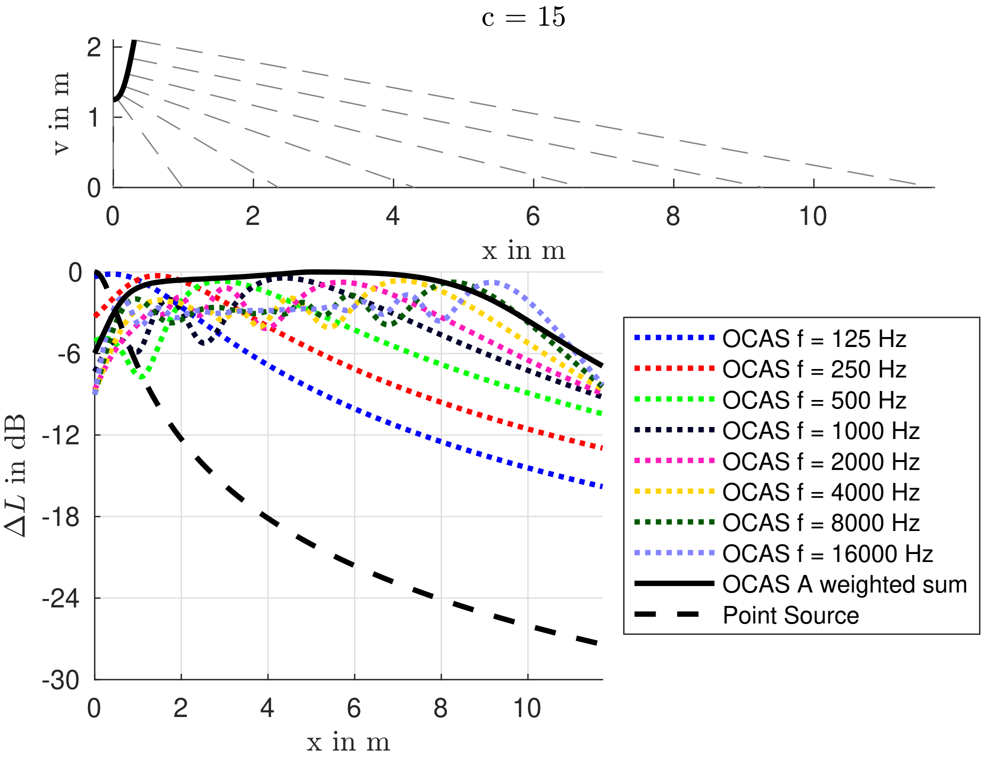

Figure 3.9 – OCAS Contour with normals connecting the source with the points of observation calculated with $v(0) = 1$, but positioned at $v_0 = 1.25$ (top) and coverage behaviour for different frequencies as well as A-weighted sum (bottom).

the slightly v-shifted version it is $3.4\,\mathrm{dB}$. A slight shift of the source into the positive v direction may improve the loudness at the far ends of the audience area. Shifting in v direction does not affect the roll off at both ends. Therefore one have to keep in mind that walls at the boundaries of the listening plane will play an essential role when assuming an indoor situation with a wall at $x_r = 11\,\mathrm{m}$. With the original version it will be exposed by a relative level of $-8.6\,\mathrm{dB}$ while in the shifted version this level is $-5.5\,\mathrm{dB}$.
Therefore it is summarized that slightly shifting the source in v direction may improve the direct-sound level for the farther listening area while simultaneously reducing it for the nearer area. Indoors, it might be essential to avoid hinting the far back fall with unattenuated sound, and hereby to avoid hanging an OCAS or line-source array too high.

Not only positive v shifts are interesting but also shifts into the negative v direction can occur. As expected, this alignment bends the frequency dependent curves into the opposite direction, cf. figure 3.10. The desired audience area of $10\,\mathrm{m}$ length is not reached anymore by the normals, as shown at the top diagram in figure 3.10. The A-weighted curve decreases for points of observations from $1\,\mathrm{m}$ to $5\,\mathrm{m}$ by $1\,\mathrm{dB}$, followed by a strong decrease up to $9\,\mathrm{m}$. Consequently the $6\,\mathrm{dB}$ condition is not met at $x_r = 8\,\mathrm{m}$ anymore.
Therefore it should be mentioned that shifting into the negative z direction will result in a reduction of the coverage so that the ends are less well supported. An OCAS that is placed too low can help if a slight decrease of the direct-sound level over distance is desired.

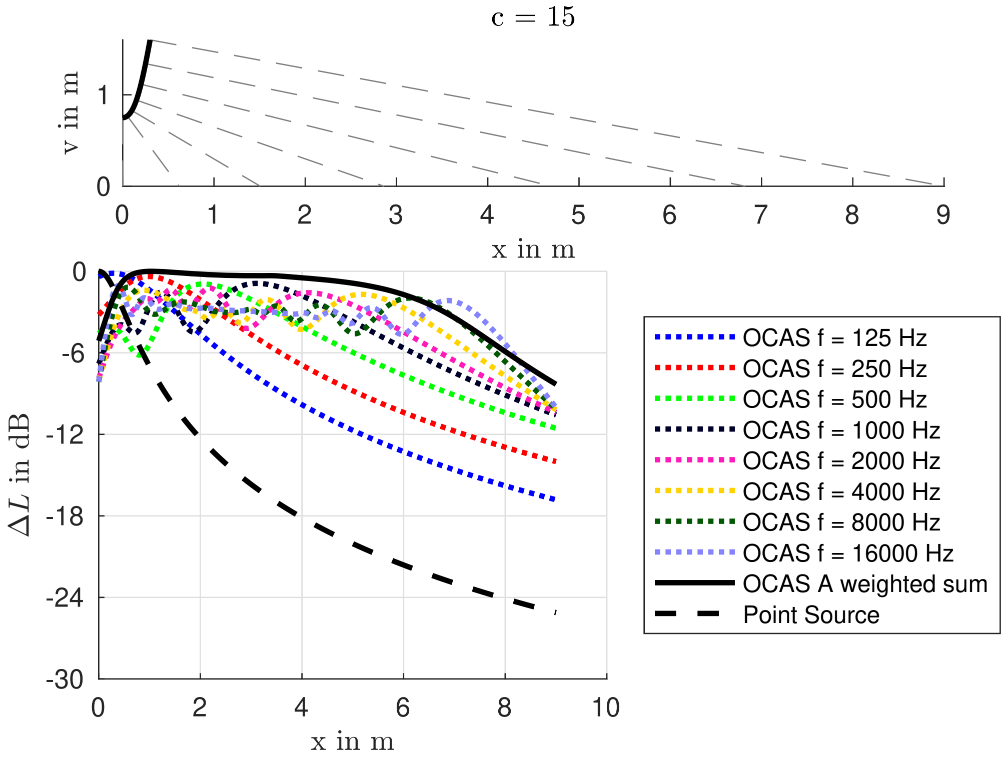

Figure 3.10 – OCAS Contour with normals connecting the source with the points of observation calculated with $v(0) = 1$, but positioned at $v_0 = 0.5$ (top) and coverage behaviour for different frequencies as well as A-weighted sum (bottom).

Not only a shift in the v coordinate can occur as an unintended configuration but also a rotation of the source as a whole. To inspect what happens by a 3° rotation, figure 3.11 is considered. Rotating by a positive angle seems to yield a wider coverage, but due to the rotation the distances between nearby points of observations are spread out. Looking at the A weighted sum the result is similar to shifting into the negative v direction.

Due to the facts that rotating and shifting along the v axis yields contrary results, one may try to combine both. Figure 3.12 shows that both effects, rotation and v shift, may cancel each other and resemble designing a new source with different settings for c, v and v'.

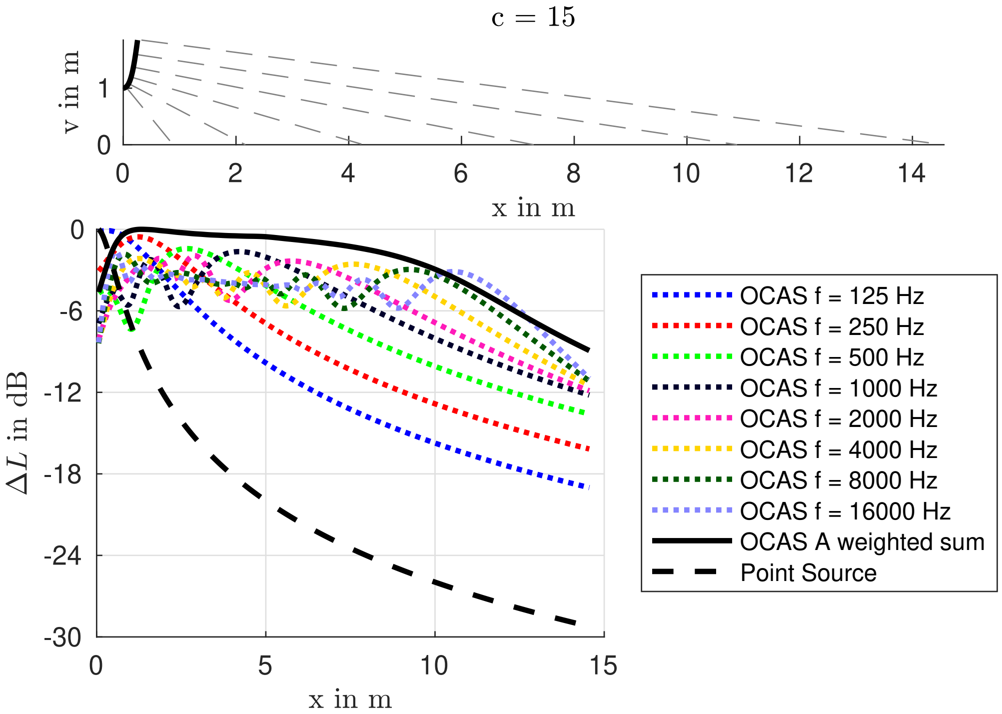

Figure 3.11 – OCAS Contour with normals connecting the source with the points of observation rotated by 3° around the y-axis (top) and coverage behaviour for different frequencies as well as A-weighted sum (bottom).

3.4 OCAS shape with Line Source Array Elements

How does the OCAS design outperform with line-source elements which are often used for large scale sound reinforcement? This question requires further investigation.
As a first example, we assume a classical, non immersive sound reinforcement scenario. Two line-source arrays may be placed left and right of a stage at the center. The size of the audience area is $30\,\mathrm{m} \times 30\,\mathrm{m}$. For this simulation the audience area is at height $1.6\,\mathrm{m}$. This is used as target height for simulations with standing audience in Nexo NS1 [23]. For rigging a $6\,\mathrm{m}$ stand is available so that a maximum distance of $6\,\mathrm{m}$ between the highest point of the array and the floor may be reached. For each side there is a maximum of six line-source elements, L'Acoustics KARA II [24], available. Figure 3.13 shows this setup from the front view as a screenshot of L'Acoustics simulation software Soundvision [25]. As the audience area should be covered optimally the sources are placed $10\,\mathrm{m}$ away from the edges.

In the next step we try to solve the differential equation so that the length of the source nearly matches the height of the six line-source elements. Next the resulting contour has to be discretized using the height of one element, $0.252\,\mathrm{m}$. At this point one have to be careful because the source is limited by the cabinets of the upper and the lower element, so that the first discretized point on the contour has to be calculated by half the height

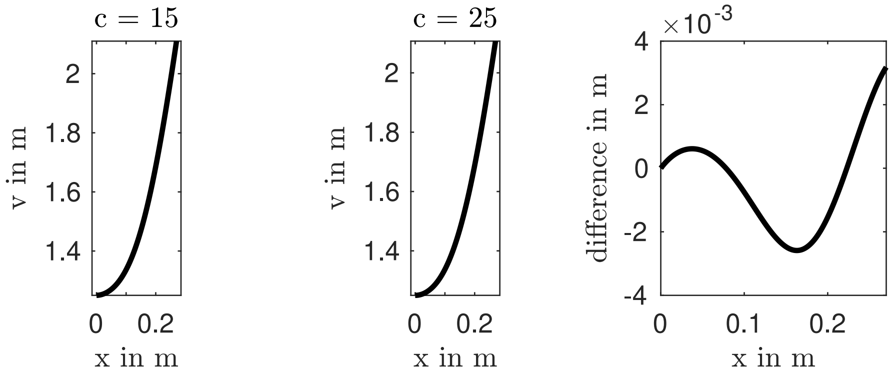

Figure 3.12 – OCAS with $c = 15$, but shifted by $0.25\,\mathrm{m}$ and rotated by 2° (left), OCAS with $c = 25$ (center) and difference of y-values (right).

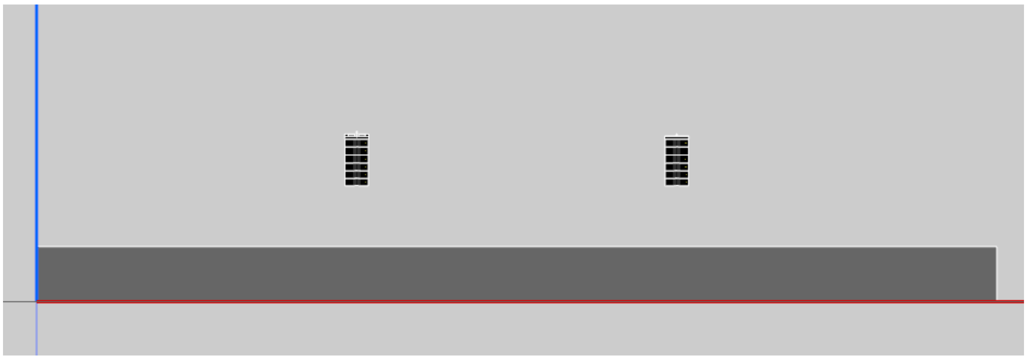

Figure 3.13 – Front view as screenshot from L'Acoustics simulation software Soundvision for stereo sound reinforcement.

of the cabinet, i.e. $0.126\,\mathrm{m}$. As a classical calculation in MATLAB is bulky, the web-based solver of the differential equation[1] using Euler's Method of (2.18) is used. The parameters to solve the differential equation can be easily modified by sliders. Figure 3.14 shows the parameters as well as the contour plotted at the webpage and the resulting points of observation for the above mentioned requirements.

In Soundvision we try to setup the line-source elements so that the points of observation are met as accurately as possible. Table 3.1 shows the resulting points of observation in the simulation software. It is not possible to set the points of observation exactly to the theoretically calculated ones because the resolution of the angle between the different line-source array elements is finite.

Figure 3.15 and 3.16 show the resulting level maps of the simulation done in Soundvision and a simulation in EASE as the interference of multiple point sources placed on the calculated OCAS contour. For two active sources of the stereo arrangement it is conspicuous that the setup by real sources cover a larger area than a simulation based on point sources do. This effect is also noticeable by considering the maps for a single source but it is not as distinctive.

---

[1] `https://lukas_goelles.iem.sh/ocas_web/`

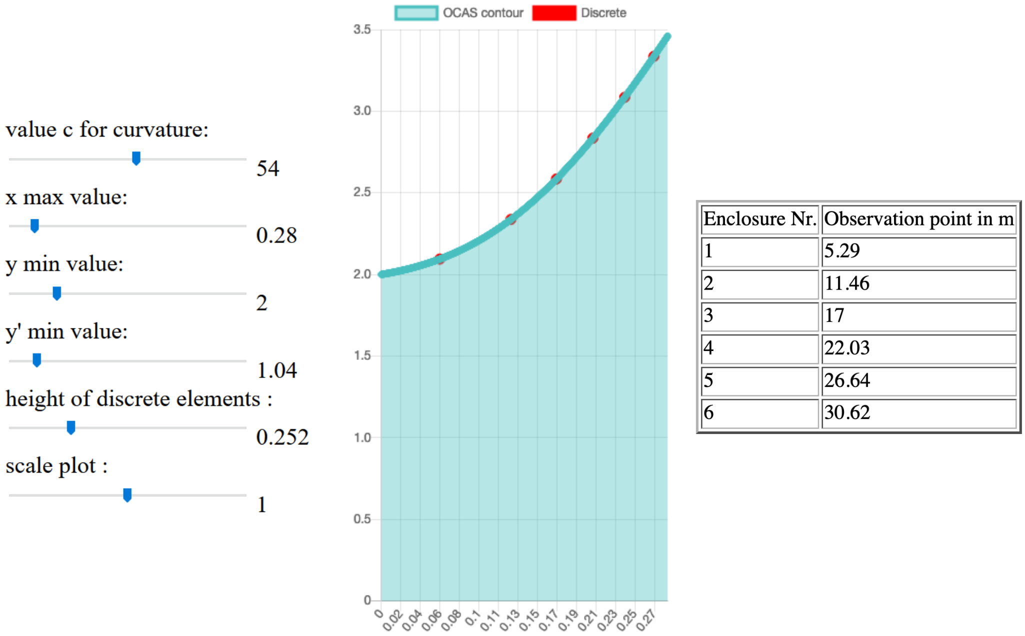

value c for curvature: 54

x max value: 0.28

y min value: 2

y' min value: 1.04

height of discrete elements : 0.252

scale plot : 1

Enclosure Nr.	Observation point in m
1	5.29
2	11.46
3	17
4	22.03
5	26.64
6	30.62

Figure 3.14 – Web-based differential equation solver of equation (2.10) using Euler's Method, equation (2.18), solved for an audience area of 30 m length, showing the parameters on the left side, the resulting shape in blue as well as the discretized points in red and the table with the resulting points of observation of the discretized version on the right.

Therefore it should be noted that the solution of the differential equation (2.10) can be used for setting up line-source arrays.

Already here the localization for panning directions between both sources is interesting to consider. For modelling the localization error the extended $\boldsymbol{r}_E$-vector model turns out to be helpful [26]. As the precedence effect should not be disregarded, it requires own weights, which are described detailed in [27]. Therefore the $\boldsymbol{r}_E$ vector is defined as

$$\boldsymbol{r}_E = \frac{\sum_{l=1}^{L} \left((1-\alpha)\, w_{p,l} + \alpha\, w_{\tau,l}\, w_{r,l}\, g_l\right)^2 \boldsymbol{\theta}_l}{\sum_{l=1}^{L} \left((1-\alpha)\, w_{p,l} + \alpha\, w_{\tau,l}\, w_{r,l}\, g_l\right)^2}\,, \tag{3.10}$$

where L corresponds to the number of loudspeakers and $\boldsymbol{\theta}_L$ to the vector pointing from the corresponding point of observation to the according L-th loudspeaker. The weight $w_{r,l}$

Enclosure Nr.	Observation point in m
1	5.29
2	10.58
3	17.4
4	21.44
5	27.57
6	29.87

Table 3.1 – Points of observation of the resulting line-source array in Soundvision.

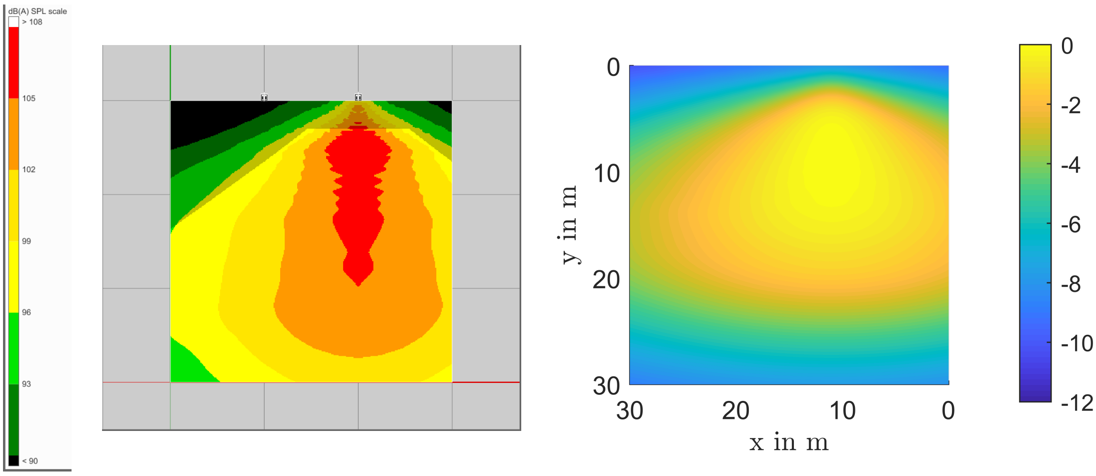

Figure 3.15 – Resulting coverage for an OCAS shape like line-source array, simulated by Soundvision with six KARA II (left, Grid: $10\,\mathrm{m} \times 10\,\mathrm{m}$) compared to a simulation as interference of multiple point sources (right).

incorporates the attention of the source propagation while $w_{\tau,l}$ models the delay between multiple sources by using the echo threshold of $-0.25\,\frac{\mathrm{dB}}{\mathrm{ms}}$ [28],

$$w_{\tau,l} = 10^{\frac{-1000}{4\cdot 20}\tau_l}, \tag{3.11}$$

where the delay is calculated by $\tau_l = \frac{c}{r_l}$. To read further informations about the calculation of the weights for the precedence effect $w_{p,l}$ the reader is referred to Eric Kurz's paper about the prediction of the listening area based on the energy vector [27]. The simple model without considering the precedence effect, i.e. $\alpha = 1$, was already successfully applied for various predictions of the listening area, for example [13], [27]. Here the extended model also considering the precedence effect is used, i.e. the linear blending parameter is set to $\alpha = 0.5$. To show the slight advantage of the new OCAS in contrast to conventional loudspeakers, figure 3.17 shows the comparison of the mean absolute localisation error for the OCAS as interference of multiple point sources and the mean absolute localisation error for a single point source located at the centre of each OCAS. It turns out that the OCAS produces a noticeably greater area for localisation errors smaller than $10\,^{\circ}$.

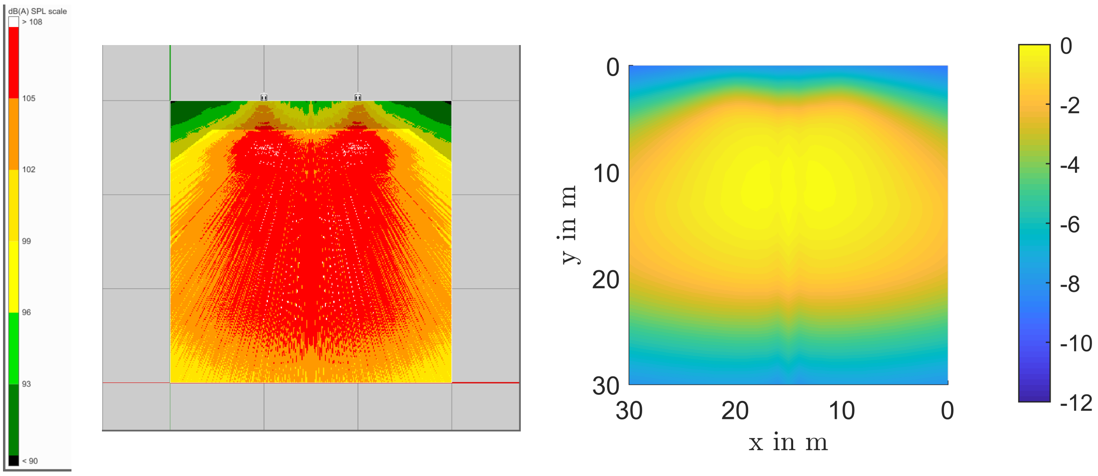

Figure 3.16 – Resulting coverage for an OCAS shape like line-source array in a stereo setup, simulated by Soundvision with six KARA II (left, Grid: $10\,\mathrm{m} \times 10\,\mathrm{m}$) compared to a simulation as interference of multiple point sources (right).

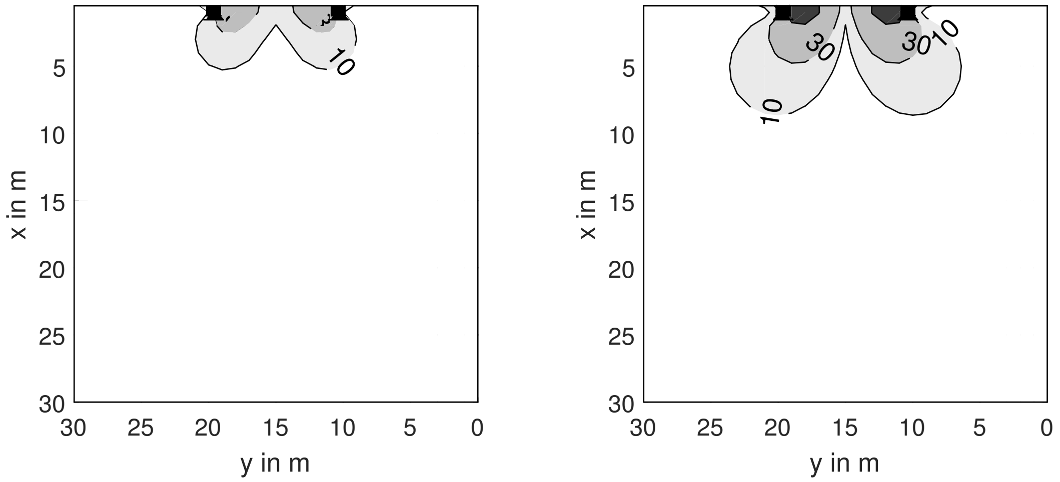

Figure 3.17 – Mean average localisation error in degrees for a stereo arrangement of 2 OCAS (left) and two point sources (right).

3.5 OCAS for 3D sound reinforcement

The OCAS simulated before are candidates for sources placed at the horizon. As there are also sound installations that require a 3D sound system, one would also try to build up an OCAS arrangement for those applications. For example the annual S3DAPC event (Student 3D Audio Production Competition [29]) deals with submissions in Ambisonics, a 3D audio recording/playback environment. To host a large audience, the new OCAS is helpful to maintain the directional balance until the outmost listening positions in the audience. We desire to plan a 3D sound system for an audience area of $30\,\mathrm{m} \times 30\,\mathrm{m}$. The setup should contain four different height layers at the elevation angles of approximately 0°, 30°, 60° and 90°. We restrict ourselves to design a system that should be as small as possible. The source height is limited to $1.5\,\mathrm{m}$ which corresponds to the height of six L'Acoustics KARA II line-source elements [24]. The loudspeaker positions of such a setup is shown in figure 3.18.

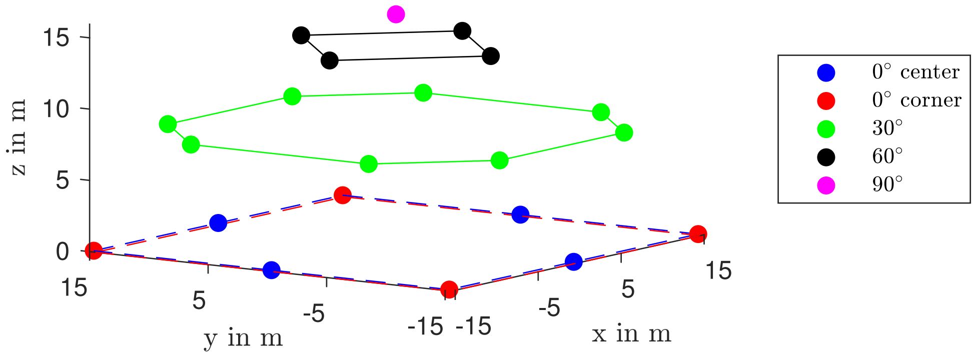

Figure 3.18 – 3D setup with four height layers at elevation angles of approximately 0°, 30°, 60° and 90°.

Table 3.2 shows the settings for each source to solve the differential equation. The setting for v, v' and x_r refer to $x = 0$. For the loudspeakers along the horizon, two different types are necessary because the sources at the corners should be able to cover larger, diagonal distances of $\sqrt{2 \cdot 30\,\mathrm{m}^2} \approx 42\,\mathrm{m}$ than the perpendicular ones ($30\,\mathrm{m}$) of the sources at the center. For the layers 30°, 60° and 90° the differential equation has to be evaluated also for negative x values to cover the whole audience area. To this end, the differential equation is first solved for positive x values followed by the negative ones. After evaluating the solution, the source has to be shifted in the xy plane to the correct position as displayed in figure 3.18.

The resulting shapes as well as the normals connecting the sources with the points of observation are shown in figure 3.19, the corresponding level maps in 3.20. The level maps are only shown once for each layer because the other may be computed by symmetry.

Considering the level maps, one would be curious to have a look at the mean average localisation error. As done already in the previous section, the extended $\boldsymbol{r}_E$ vector model, respecting weights for the precedence effect, is used therefore again. Encoding is done by spherical harmonics as described in [13]. The AllRAD (all-round Ambisonic decoding)

Source	c	$v(0)$	$v'(0)$	$x_r(0)$
0° center	32	1	2	2
0° corner	45	1	2	2
30°	180	7.8	0	0
60°	330	13	0	0
90°	290	14	0	0

Table 3.2 – Settings for solving the differential equation for each layer of the 3D setup shown in 3.18.

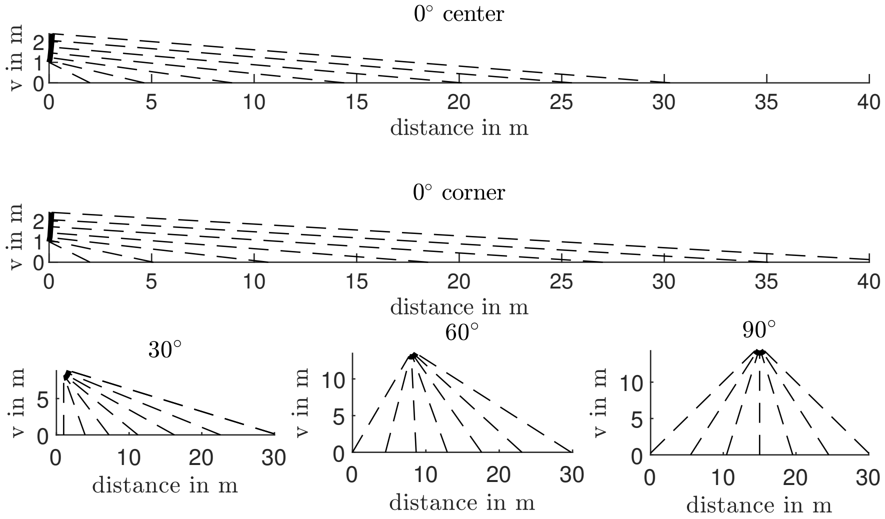

Figure 3.19 – Shape and normals connecting the points of observation with the contour of the sources for each layer.

decoder allows to decode an Ambisonic signal for a custom loudspeaker arrangement [30]. As [31] describe the negative effect of delay compensated systems on the sweet area, only amplitude compensation to a central listening position at $x = y = 0$ is done.

Figure 3.21 shows the mean average localization error for an arrangement of OCAS sources for a fifth order Ambisonic playback scenario along the horizon compared to conventional loudspeakers, modelled as point sources. Although it is mentioned in [13] that applying max $\boldsymbol{r}_E$ weights will affect the listening area positively, a decisive difference between the basic version and the version with applied max $\boldsymbol{r}_E$ weights cannot be seen in this setup so that the maps with applied max $\boldsymbol{r}_E$ weights are not shown here.

An approach considering the plausible sweet area is mentioned in [32]: The audience area is therefore defined as $\frac{2}{3}$ of the radius of the setup assuming the Ambisonic playback order is high enough. As this model is valid for point sources, we have a look at the mean average localisation error for the point-source arrangement. At a radius of $10\,\mathrm{m}$, which corresponds to $\frac{2}{3}$ of the setup radius, the 10° mark is reached for loudspeakers at 0°, 90°, 180° and 270°. Searching this mark in the OCAS simulation will yield a radius of $14.5\,\mathrm{m}$. In this way only very close to the sources the mean absolute localization error is noticeable high. This mark has to be reduced to $13\,\mathrm{m}$ as the initial condition of

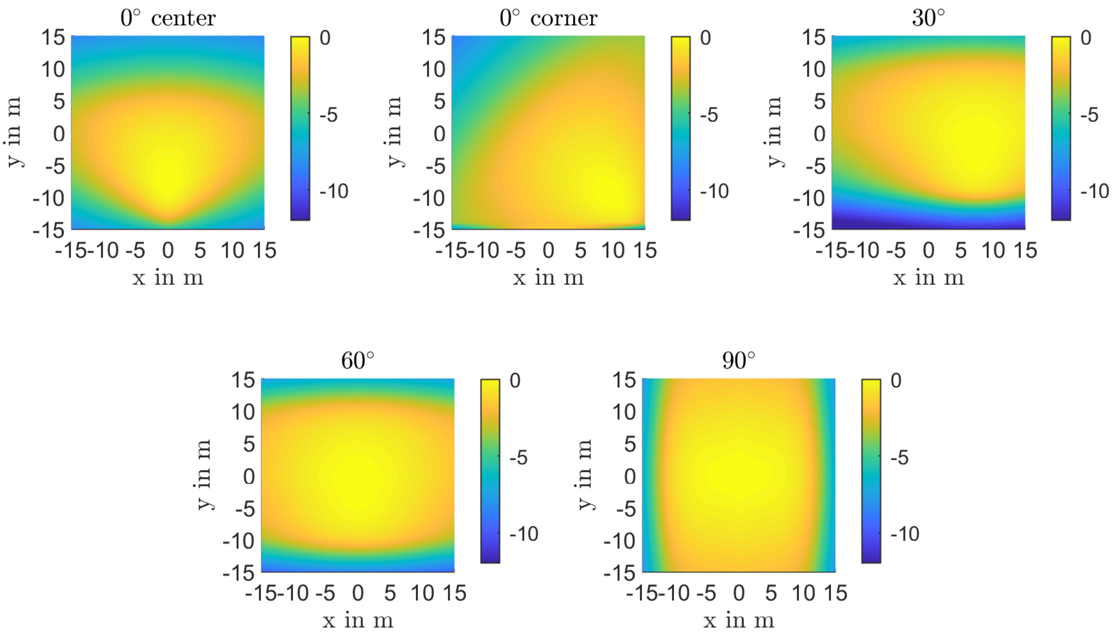

Figure 3.20 – Level map for each layer.

the differential equation v' was set to 2, which yields a first point of observation of $2\,\mathrm{m}$. Therefore we can conclude that the plausible listening area for the OCAS setup is limited by the choice of the initial conditions and the resulting points of observation. For the OCAS a rectangular sweet area of $26\,\mathrm{m}$ $\times$ $26\,\mathrm{m}$ ($676\,\mathrm{m}^2$) may be found for which the error stays below $10\,^\circ$. For the point source arrangement, the rectangle is defined by $20\,\mathrm{m}$ $\times$ $20\,\mathrm{m}$ ($400\,\mathrm{m}^2$), which yields a factor of 1.69 in between the resulting areas. Another interesting point of view is to define those areas as ratio between the plausible sweet area and the whole predefined audience area. This yields an exploitation of $44.44\,\%$ by using a point source arrangement which is increased to $75.11\,\%$ by using an OCAS arrangement. The expected benefits are assumed to be most noticeable at listening positions at the outer rims of the seating area.

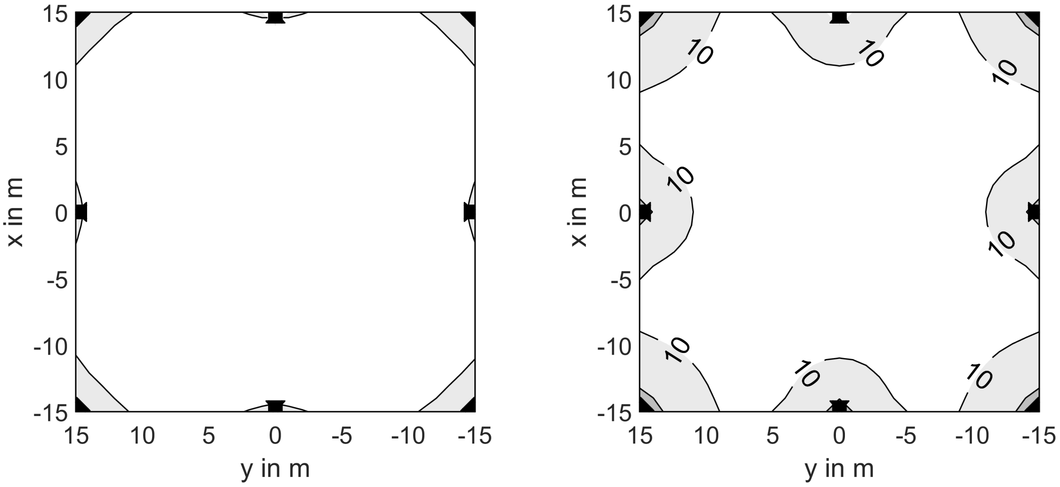

Figure 3.21 – Mean average localisation error for panning along the horizon for an arrangement with OCAS (left) compared to an arrangement with point sources (right).

As in the previous section, we try to model the OCAS shape by line-source elements. As the height is limited by $1.5\,\mathrm{m}$, we are able to use six L'Acoustics KARA II [24] line-source loudspeaker elements for the simulations. First we build the horizontal layer without any problems. We denote that the nearest point of observation is not reached completely due to the finite precision of the angle between the elements cf. figure 3.22. By contrast to figure 3.20 that shows the simulation as an interference of multiple point sources, the coverage of the line-source array is narrower due to the radiation behaviour of the real sources.

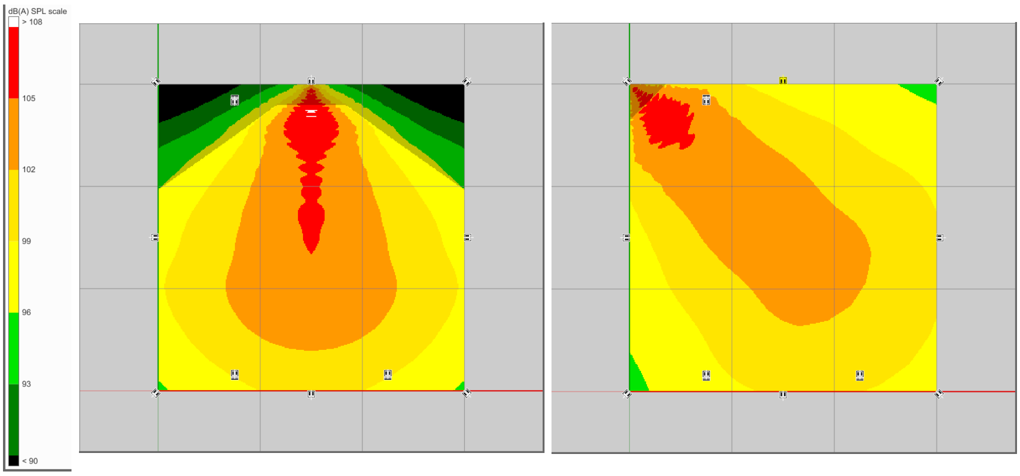

Figure 3.22 – Simulated A-weighted level maps by Soundvision for an OCAS shape like line source array build of six L'Acoustics KARA II for the layer on the horizon.

For the higher layers we desire that points of observations behind the x position of the source are also covered what makes modelling the OCAS shape by line-source elements difficult. It is not possible to set up a source that is able to play in both directions (front and back) because of the upper splay-angle limit of 10° between line-source cabinets. Alternatively, one may build up the source for the second layer (30°) by taking only 5 elements so that only the frontal part is considered, cf. figure 3.23. This compromise cannot be applied for the reaming layers. Either complex constructions are necessary or a new source with the presented waveguide from chapter 2.3 has to be used.

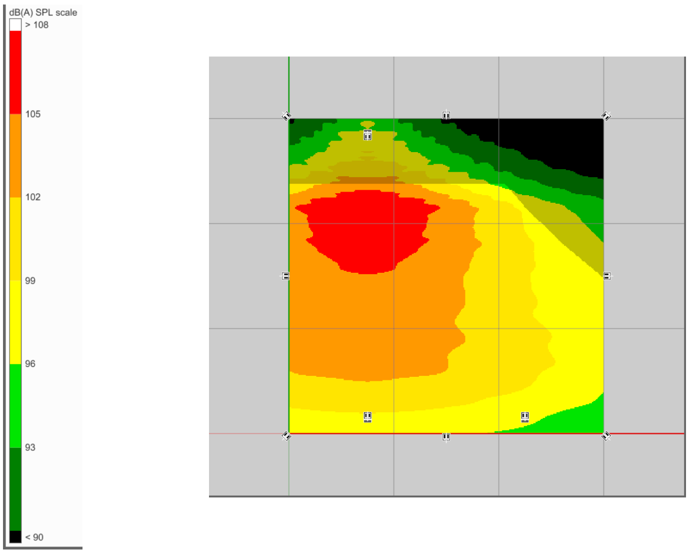

Figure 3.23 – Simulated A-weighted level map by Soundvision for an OCAS shape like line source array build of six L'Acoustics KARA II for the 30° layer.

Summarizing it should be noted that line-source arrays can be set up following the OCAS shape if stereo sound reinforcement or immersive sound reinforcement along the horizon is targeted as application. When dealing with three-dimensional setups, the typical, professional line-source elements reach their configuration limits when trying to shape the higher layers. More compact solutions appear to be infeasible with typical line-source arrays, in practice. For such purposes, the waveguide presented in chapter 2.3 appears more appropriate.

Chapter 4

OCAS Waveguide prototype/ proof of concept

4.1 Prototype layout

In this chapter, a prototype of the OCAS discussed before is 3D-printed and reviewed. The purposed waveguide is printed by a conventional 3D printer, Prusa I3 MK3S+ [33]. The printer is only able to print elements of a maximum size of $0.25\,\mathrm{m} \times 0.22\,\mathrm{m} \times 0.2\,\mathrm{m}$. Therefore the 3D printed waveguide has to be compact to print as few elements as possible which have to be glued together finally.
The room for which the design should work is the IEM CUBE, a $10.3\,\mathrm{m} \times 12\,\mathrm{m} \times 4.8\,\mathrm{m}$ studio with reverberation time of $0.5\,\mathrm{s}$. Employed as high frequency transducer of a horizontal loudspeaker, the OCAS should be able to cover a distance of approximately $9\,\mathrm{m}$. We choose to design a source which is placed at the horizon. The first seat row is placed at $x_R = 0.5\,\mathrm{m}$ which yields the initial condition for the first derivative $v' = 1$ by choosing $v = 0.5$. A curvature/distance parameter of $c = 15$ will do the job of an optimal coverage of a distance of approximately $9\,\mathrm{m}$, cf. figure 4.1.

As the source is not extended much in v direction, we cannot presume that the frequency response over distance is flat for a wide frequency band. In chapter 3.2 the influence of the source height on the frequency dependent near and far field was discussed. Figure 4.2 shows the frequency dependent coverage. For low frequencies there is no difference between the OCAS and a point source. The designed OCAS will only be effective for

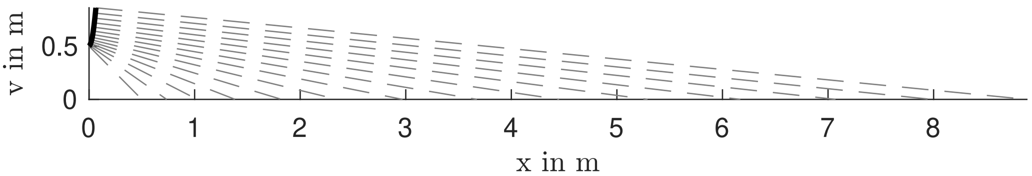

Figure 4.1 – Resulting shape of the OCAS for the IEM CUBE with normals connecting the points of observation with the contour.

higher frequencies. The influence will be clearly visible above a frequency of $1\,\mathrm{kHz}$. For this small source the influence of the geometry can be considered closer, as the stationary phase approximated integral is interrupted too fast in both directions.

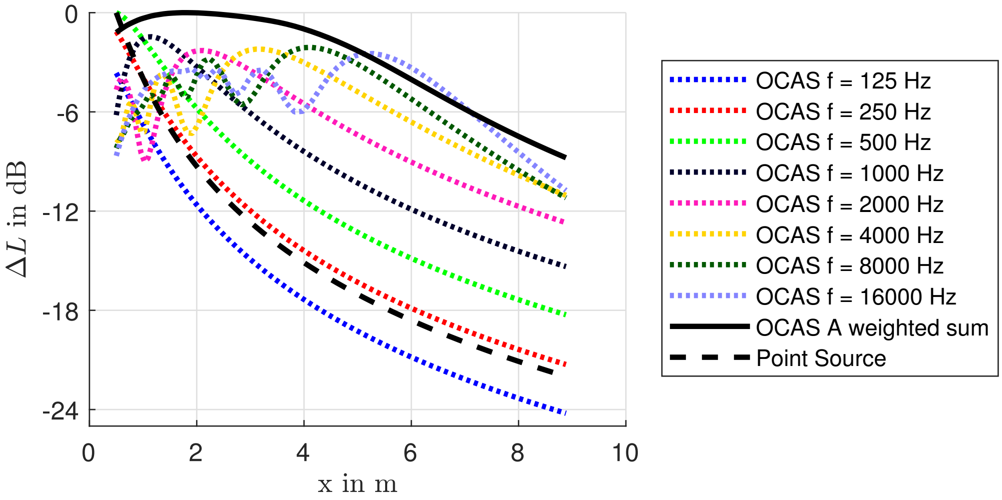

Figure 4.2 – Frequency dependent coverage of the OCAS designed for the CUBE compared to a single point source.

It is not meaningful to build a prototype of a full-band system, therefore we focus on the $> 1\,\mathrm{kHz}$ frequency range to prove the OCAS concept. To support this operation range we use a single compression driver, SB Audience BIANCO-44CD-T [34], which promises a frequency range from $700\,\mathrm{Hz}$ up to $20\,000\,\mathrm{Hz}$. Figure 4.3 shows the A weighted sum of the theoretical model, over an audience area of $10\,\mathrm{m} \times 10\,\mathrm{m}$.

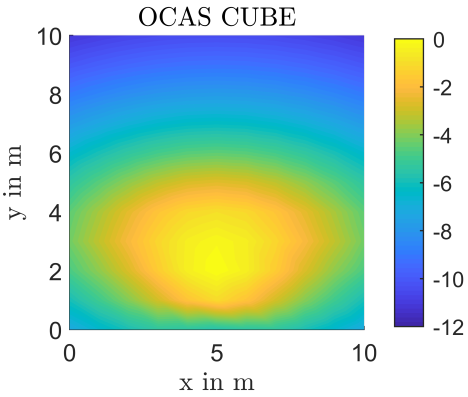

Figure 4.3 – Simulation: Map of the A-weighted sum for the prototype

As the shape is defined, the next step is to think about designing the waveguide prototype. Chapter 2.3 discusses the modelling by using polynomials in detail. To avoid bending the waves extremely in the xy plane of the waveguide, the depth of the construction has to be considered further. The length of the output for the CUBE OCAS is approximately $38\,\mathrm{cm}$. The height of the cone h_c is set to $9.5\,\mathrm{cm}$. The cone is therefore big enough to guide the waves sufficiently along this cone before the polynomials starts. The height of the second cone $h_{c,2}$ is set to $19\,\mathrm{cm}$. Executing the proposed procedure yields the interior body of the waveguide, cf. figure 4.4.

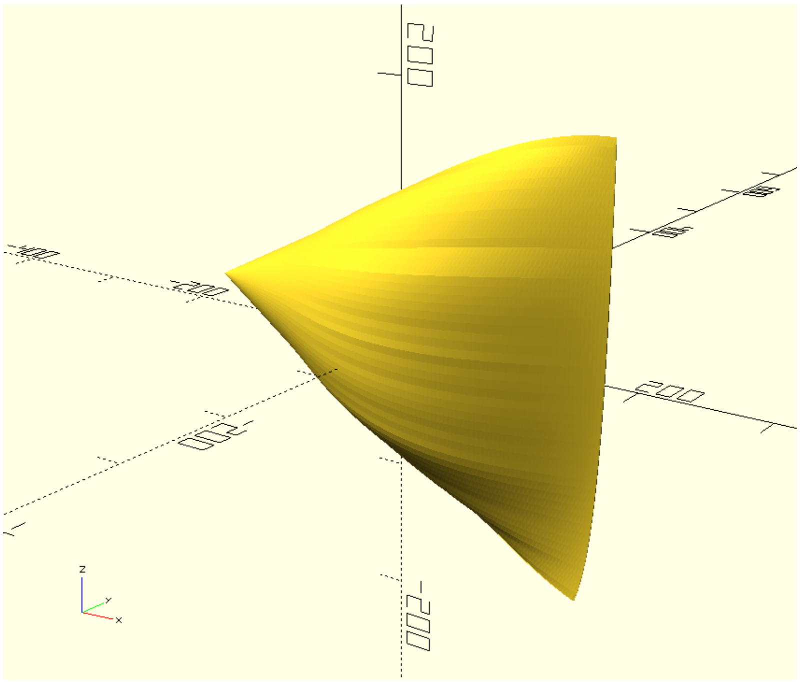

Figure 4.4 – Internal body of the resulting waveguide.

To build the external body around the internal, we choose to have a distance of $127\,\mathrm{mm}$ which corresponds to the half diameter of the compression driver. The resulting waveguide with flange for the compression driver is shown in figure 4.5 as a cut along the y axis. Figure 4.6 shows the final 3D printed waveguide with mounted compression driver. The wall thickness is hereby $2\,\mathrm{mm}$ which is thick enough to guarantee stability.

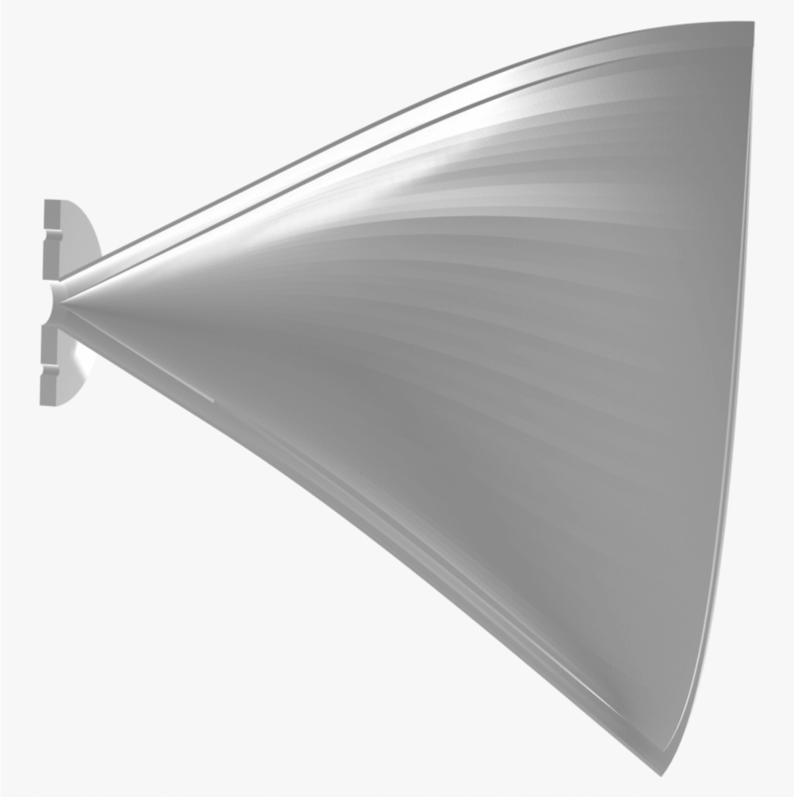

Figure 4.5 – Parallel shells between which the waves are directed with flange for the compression driver cut along the y-axis to view inside the waveguide.

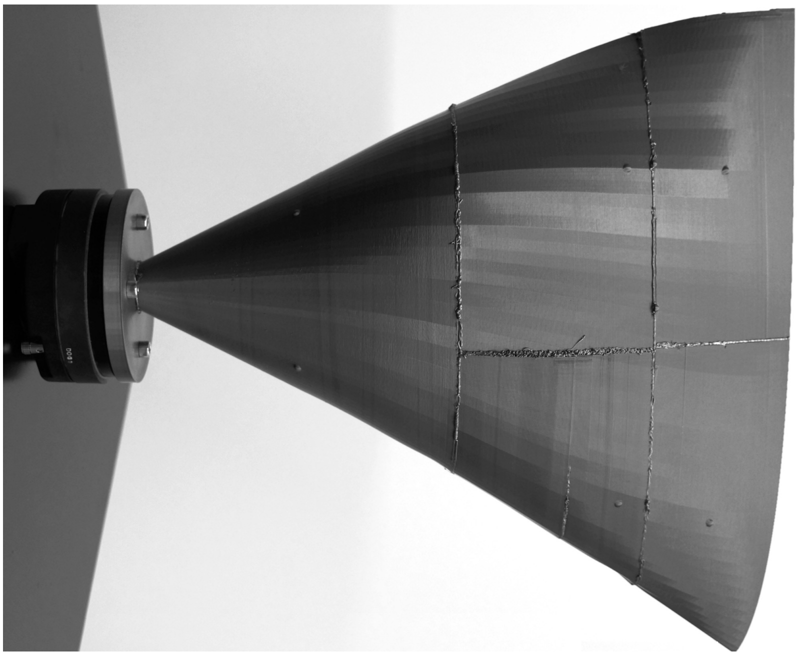

Figure 4.6 – Resulting 3D printed waveguide with mounted driver.

4.2 Measurements

4.2.1 Measurements at the waveguide output

First, our interest lies in verifying the expected wave-sculpting effect at the waveguide orifice. To this end, we review the impulse response measured at different positions at the orifice. 6 microphones are used to evaluate the impulse responses, cf. figure 4.7. These microphones are used to record the sweep response of a $5\,\mathrm{s}$ long sweep. Deconvolution and plotting was done in MATLAB. All impulses hit the output at (nearly) the same time, see figure 4.8. By further inspecting, the worst-case time difference between the impulse appears to be $1\,\mathrm{Sample}$ at a sampling frequency of $44.1\,\mathrm{kHz}$. This is equivalent to a time shift of $0.0227\,\mathrm{ms}$ that corresponds to a distance of $7.77\,\mathrm{mm}$. If this distance is assumed to be half the wavelength, the influence of this mismatch is expected to only affect a frequency around $22\,\mathrm{kHz}$. It can be concluded that the output of the waveguide serves its purpose of equalizing the path lengths so that the source is suitable to be applied for further experiments in practice.

Figure 4.7 – Impulse response measurement setup at the orifice

Before having a look at the coverage behaviour over distance, one might consider the frequency responses at the waveguide output, cf. figure 4.9. It is striking that at microphone position 3 a strong resonance is measurable for $5\,\mathrm{kHz}$. The self-printed prototype is not free of structural resonances. Especially for position 1 and 5 a damping for high frequencies is noted. For the top position this may be caused by the fact that the 3D printer was not able to print the top outlet as desired which yielded in parts glued together.

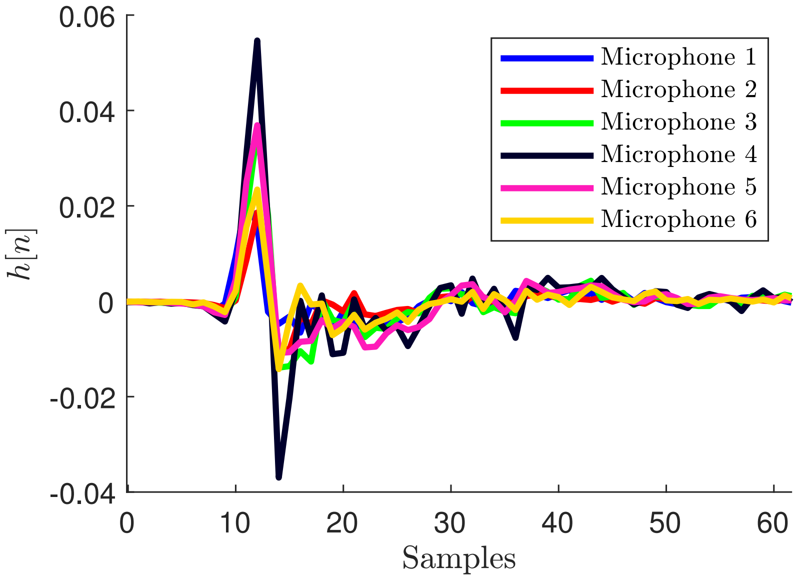

Figure 4.8 – Impulse responses at the orifice

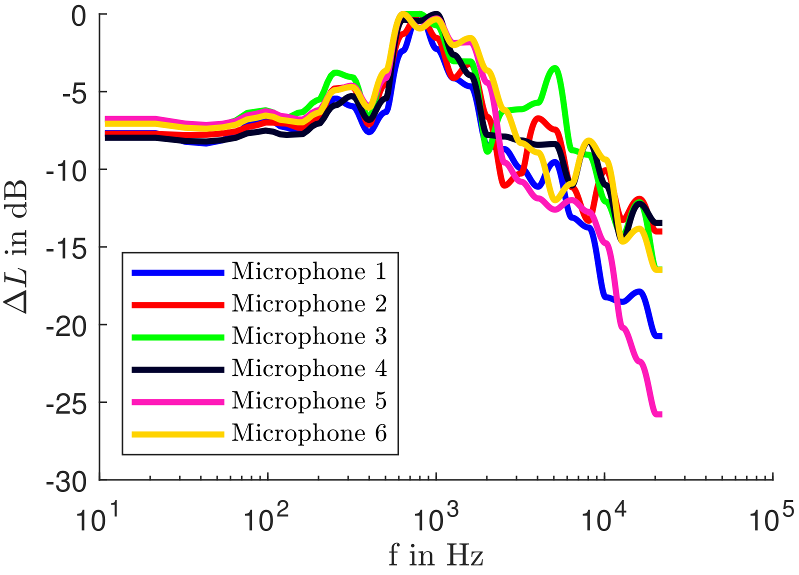

Figure 4.9 – Frequency responses at the waveguide output

4.2.2 Measurements inside the IEM Cube

For measurements at the IEM Cube, a grid of $8\,\mathrm{m} \times 3\,\mathrm{m}$ was used to evaluate the coverage behaviour, cf. figure 4.10. To compare the new OCAS to a common point-source loudspeaker, a Tannoy System 800 loudspeaker (a bit smaller than the loudspeakers that are permanently installed) is used. A NTi Audio M4261 microphone evaluates the omnidirectional room impulse responses and a Soundfield ST450 MKII was used to get Ambisonic room impulse responses for the web-based virtualization. The source was positioned $1.7\,\mathrm{m}$ above the ground and the microphones are placed $1.2\,\mathrm{m}$ above the ground to comply with the design of the OCAS prototype ($v = 0.5$).

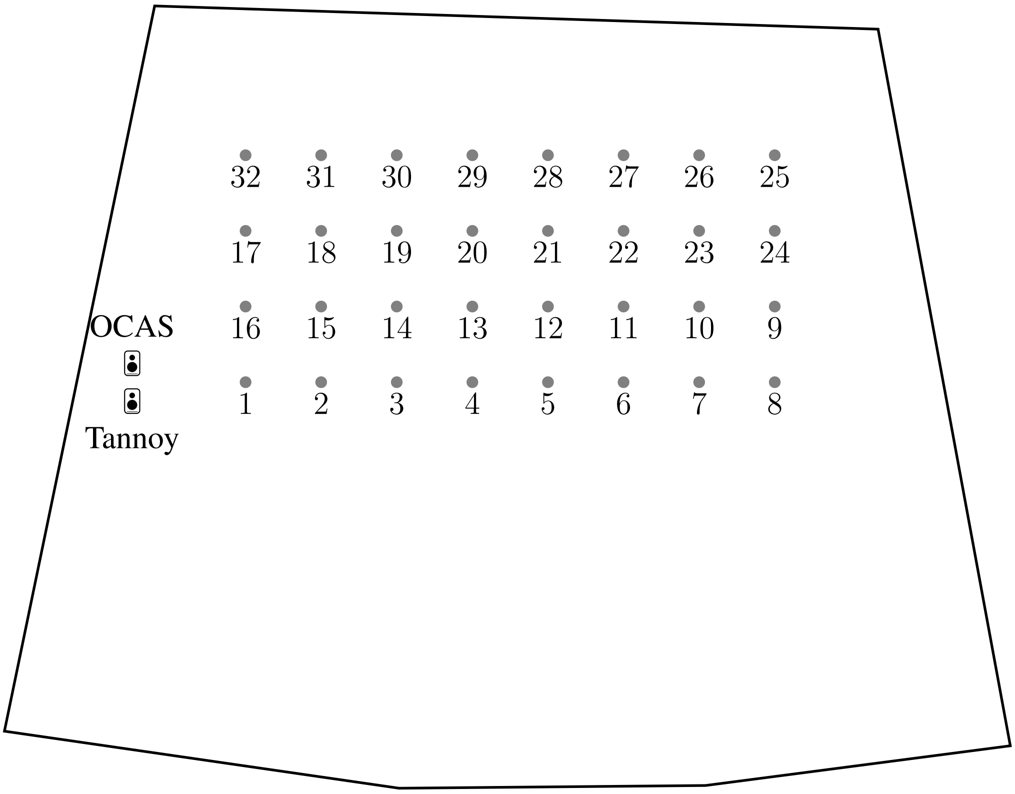

Figure 4.10 – Loudspeaker and receiver positions at the IEM CUBE

As a first evaluation, the A-weighted sum of both loudspeaker over distance is discussed, cf. figure 4.11. It is assumed that the radiation behaviour is mirror symmetric, i.e. the receiver positions can be mirrored to virtually cover a resulting area of $8\,\mathrm{m} \times 6\,\mathrm{m}$. The resulting SPL contour in the plots of figure 4.11 appear to confirm the simulation results, cf. figure 4.3, of a (nearly) equally covered area with the OCAS. By contrast, a noticeable difference at a distance of $4\,\mathrm{m}$ on-axis occurs at the map for the Tannoy speaker. Off-axis this critical distance is reduced to approximately $2\,\mathrm{m}$ - $3\,\mathrm{m}$ depending on the position. Already at this point, the expected advantage of using an OCAS stands out.

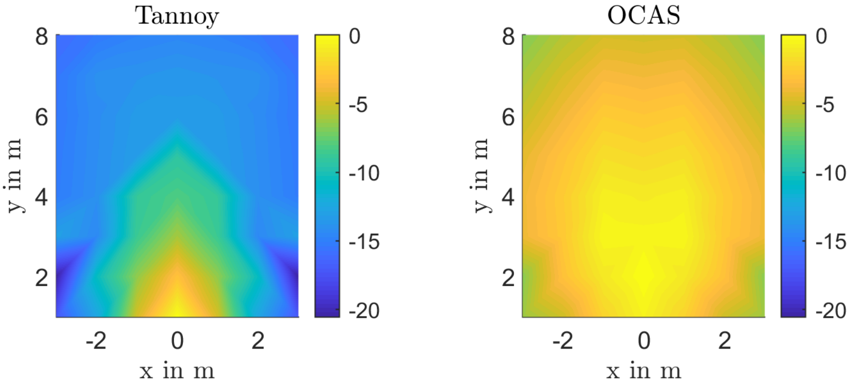

Figure 4.11 – A weighted sum of the frequency response over the listening plane for Tannoy System 600 (left) and OCAS (right)

From the chapter on simulations it is known that the A weighted sum is helpful to get an overview, and we know that the OCAS size plays an essential role in terms of frequency dependent radiation. To get an approximate overview, the level maps of double octaves are discussed next, cf. figure 4.12. Comparing to the simulation results, the coverage for the lower frequencies corresponds with the coverage of a point source. While the OCAS begins to be effective for the mid frequency double octave 1 kHz - 4 kHz, its effectiveness is highly developed for the higher frequency double octave 4 kHz - 16 kHz, resulting in a nearly constant direct-sound level. By contrast, the radiation profile for the Tannoy loudspeakers stays approximately constant for all considerations so that for higher frequencies the advantage of the OCAS is clearly visible. These results confirm the impression of a remarkably constant high-frequency SPL.

To observe the radiation behaviour in greater detail, the level maps for different third-octave averaged frequencies are considered, cf. figure 4.13. Comparing the measurements with the simulations, it turns out that the real coverage at high frequencies is better than the simulated ones, i.e. the difference between near and far are not as distinctive. While the radiation for 1 kHz still resembles a point source, the area of even direct-sound coverage, i.e. the yellow area in the plots, increases for 2 kHz. The areas supplied with uniform direct sound increases further for 4 kHz, and a decrease of amplitude for 8 kHz is denoted.

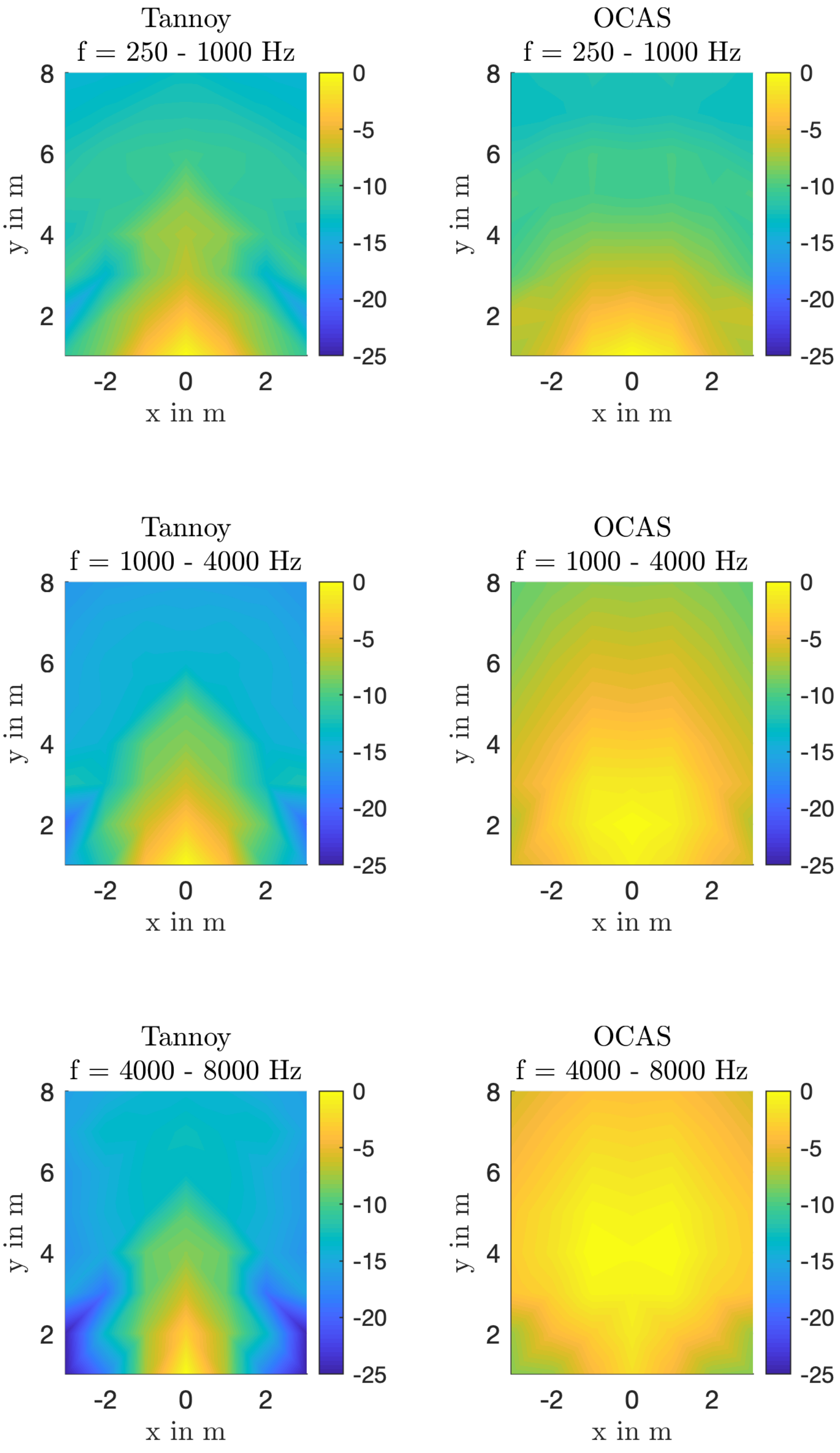

Figure 4.12 – Level maps for double octaves 250 Hz - 1 kHz (top), 1 kHz - 4 kHz (center), 4 kHz - 8 kHz (bottom) over distance for Tannoy System 600 (left) and OCAS (right), each normalized to 0 dB

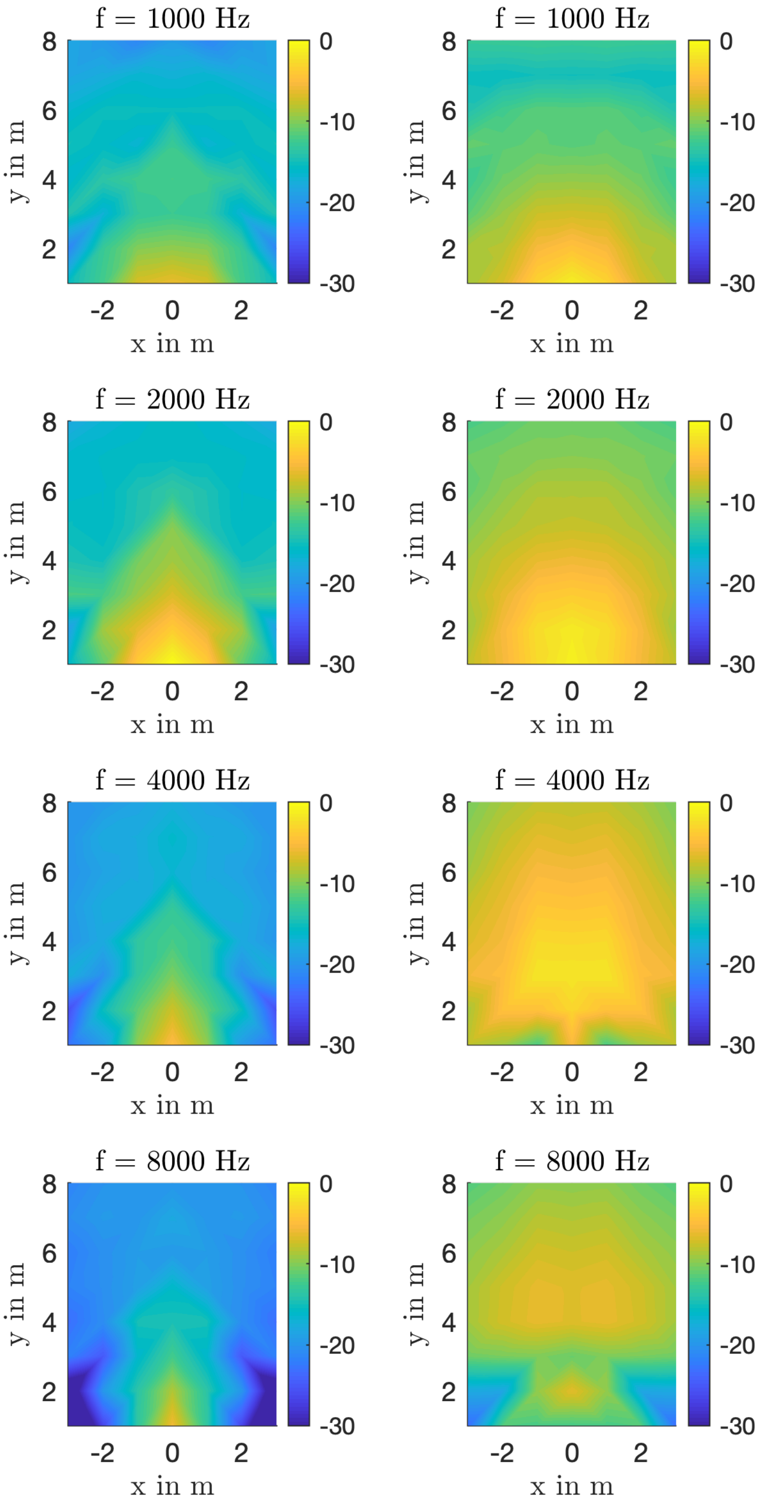

Figure 4.13 – Third-octave averaged level maps for 1 kHz (first row), 2 kHz (second row), 4 kHz (third row) and 8 kHz (fourth row) over distance for Tannoy System 600 (left) and OCAS (right)

Figure 4.14 shows the third-octave averaged direct-sound frequency response for different receiver positions enumerated as in figure 4.10. The primary feature concerns the position dependent level differences that are not as distinctively pronounced for the OCAS as they are for the Tannoy loudspeaker. For the OCAS, the measured amplitude decrease at high frequencies corresponds to $-3\,\mathrm{dB/oct}$ plus the transducer response and uniformly effects every receiver position. To get rid of it, an equalizer is needed. In the rather uniform responses of the OCAS, only position 1, which is very close to the source, sticks out.

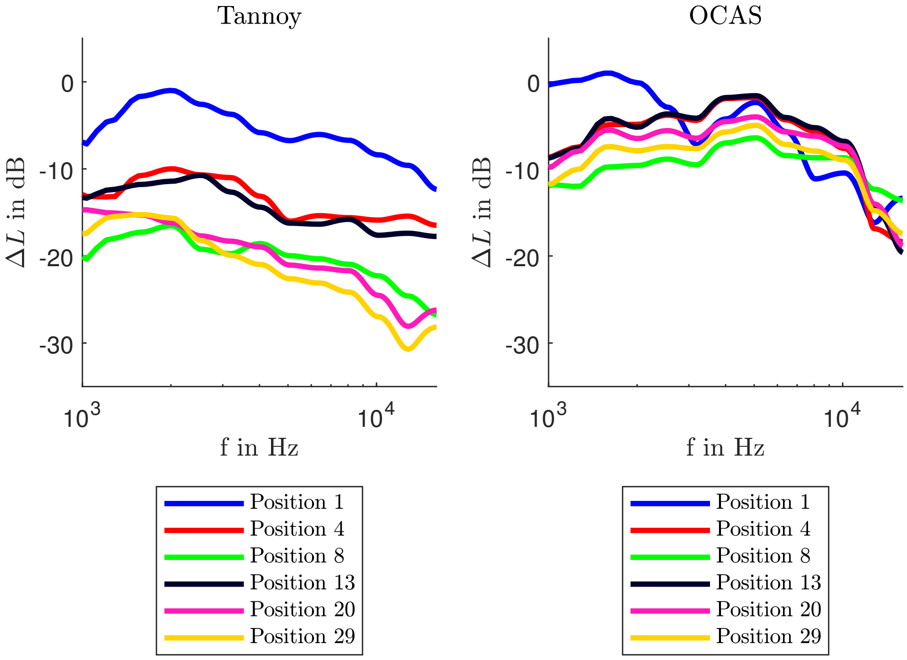

Figure 4.14 – Third-octave averaged direct sound frequency response for different positions enumerated as in figure 4.10.

Figure 4.15 shows the comparison between the simulated direct-sound level and the measured one. Due to the high-frequency roll-off of the OCAS with transducer, cf. figure 4.13, we need an equalizer to make the measured results comparable to the simulated ones. The magnitude of the used filter is shown in figure 4.16. Compared to the simulated results, the graphs of the OCAS prototype now follow nearly identical trends. For $8000\,\mathrm{Hz}$ the simulated roll-off is not as steep in the measured results. This result most distinctively confirms the applicability of the OCAS theory and waveguide design presented in this thesis.

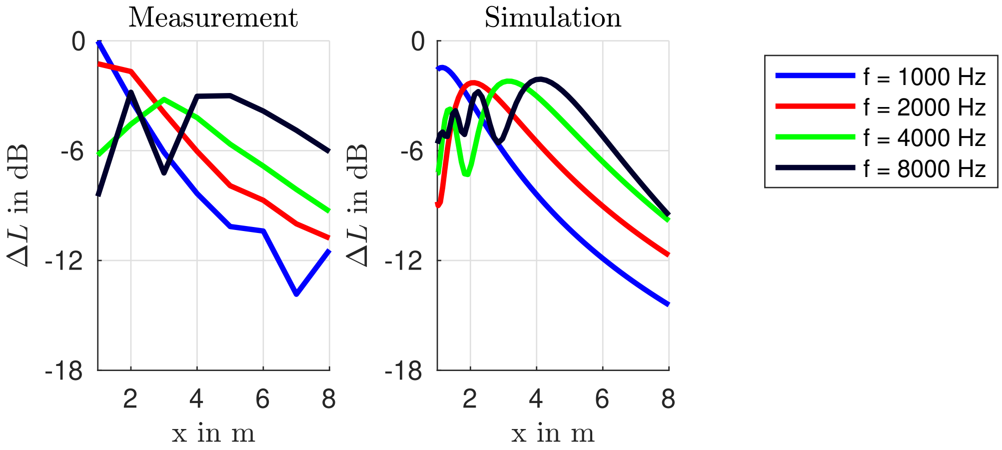

Figure 4.15 – Measured vs. calculated direct-sound level.

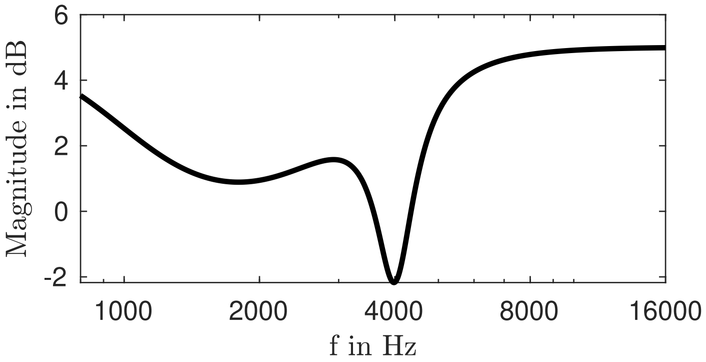

Figure 4.16 – Equalizer to make the measured results comparable to the simulated ones.

Of similar relevance, one should not forget about other important room acoustic parameters, for instance the direct to reverberant energy ratio (DRR) because it contributes to the perceived distance and to the perceived source width, as discussed in [35]. It relates the energy of the direct-sound parts of the impulse response to the diffuse parts [36],

$$\mathrm{DRR} = 10 \cdot \log \left(\frac{\sum_{\omega} |H_D(\omega)|^2}{\sum_{\omega} |H_R(\omega)|^2} \right) , \tag{4.1}$$

where $|H_D(\omega)|^2$ denotes the frequency dependent energy of the direct sound and $|H_R(\omega)|^2$ the frequency dependent energy of the reverberant sound. Figure 4.17 shows the DRR as function over the receiver positions as well as a map of the DDR over the audience area. Surprisingly the DRR always stays positive for the OCAS and only rolls off gently with distance. In contrast, the reverberant sound energy will dominate for sound reinforcement with the Tannoy loudspeaker at most off-axis listening positions.

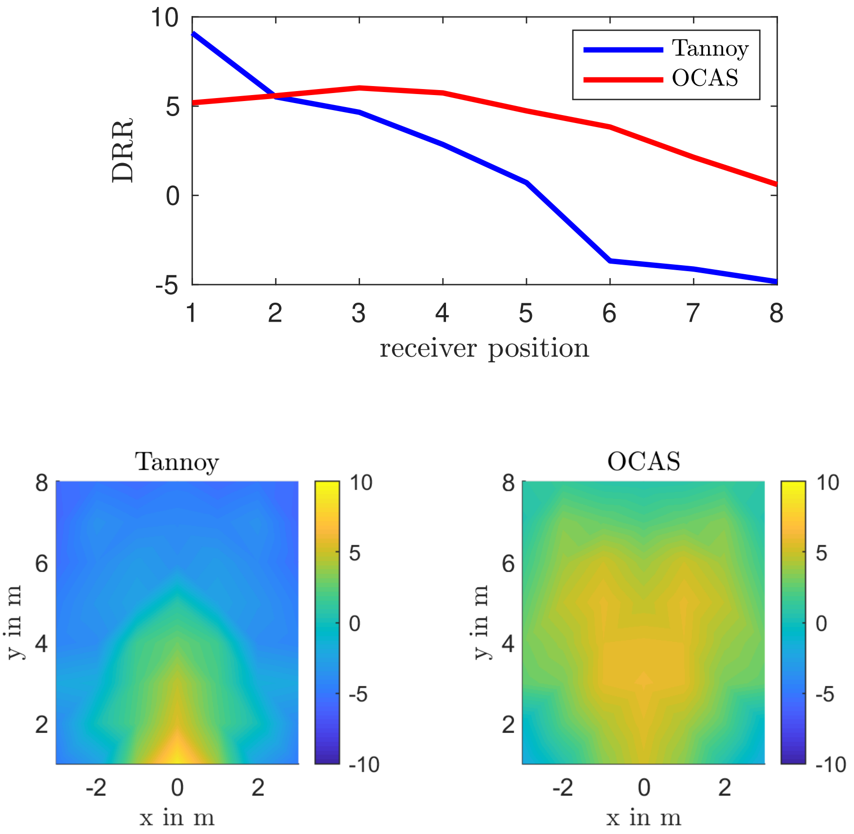

Figure 4.17 – DRR for different receiver positions comparing the Tannoy loudspeaker with the OCAS.

4.3 Virtualization

As the measurement series also contains First-order Ambisonic Room Impulse Responses, there are also responses that can be used to obtain a playback impression at different positions within a virtual OCAS array. Because chapter 3.5 describes how the new OCAS may be used for immersive sound reinforcement, a virtual immersive setup is prepared by rotating the measured source along the horizon so that a setup with eight sources results. It is already known that the resolution of direction of those impulse responses is limited. Therefore the 2DSE2 algorithm [37] is used for enhancement. To offer the possibility of moving the listener's head without additional hardware, the examples are played back by a slightly modified version of the CAT3DA-player (camera tracked 3D audio player) [38]. This player was developed for the annual festival Musikprotokoll of ORF Steiermark (Austrian Broadcasting Corporation, federal state studio Styria) to enable interactive sound installations where the user's head is tracked by the webcam of its laptop. The CAT3DA player is built upon Google's MediaPipe Face Mesh [39], the MPEG-DASH framework dash.js [40] and some of the Ambisonics processing is based on JSAmbisonics by Archontis Politis and David Poirier-Quinot [41].

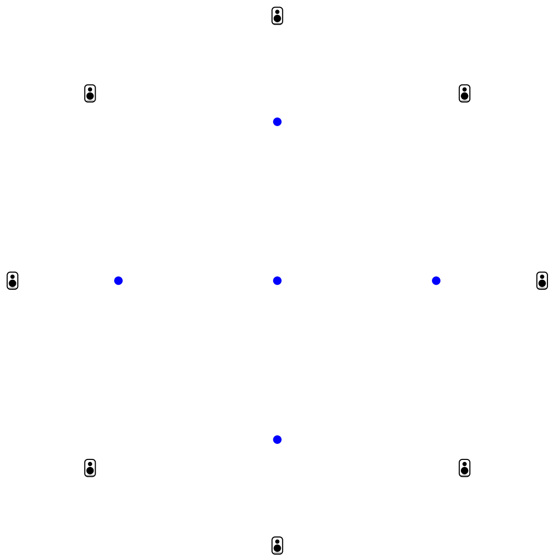

Figure 4.18 – Virtual setup with different receiver points

For each position, marked as blue dots in figure 4.18, the listener is able to switch between the virtual Tannoy setup and a processed mixture of Tannoy and OCAS where the Tannoy loudspeaker is responsible for the frequency below 800 Hz and the OCAS source above. In all cases, the listener hear an Ambisonic mix at the virtual CUBE of What's Trumps [42] played by the RhythmusSportGruppe. The example is prepared in REAPER by using the IEM plug-in suite [43], i.e. the AllRAD-Decoder and the SceneRotator as well as Matthias Kronlachner's mcfx_convolver [44]. The binaural decoder employed in the CAT3DA-player corresponds to the binaural decoder of the IEM plug-in suite, i.e. the MagLS binaural decoder [45]. Using the upmixed Ambisonic Room Impulse Responses (ARIR) of positions 1, 4, 7, 18, 22 and 29 allows to build up a virtual arrangement as shown in figure 4.18. The listening position at the center is hereby created by always using position 4 and rotating the resulting scene. For the other 4 positions, which are called front, back, left and right in the web player, combinations of the positions 1, 7, 18, 22 and 29 are necessary followed by rotating the source accordingly. As [13] purposes to use at least third order Ambisonics for a headphone playback scenario, the ARIRs are prepared at this order.

At the web player[1] it is possible to switch between the Tannoy version of the setup and a combination of the Tannoy loudspeaker and the OCAS prototype by the buttons displayed in the screenshot of figure 4.19. If the player does not recognize a webcam or the access is denied, the player works as simple binaural player. The light beside the graphical representation displays the confidence of the tracking. Green denotes good tracking, a yellow light is critical and red means that tracking is not possible, the access to the webcam is denied or the webcam is not found. Please note that the player works only for new versions of Firefox or chromium based browsers, like Google Chrome, Opera, Microsoft Edge, because playing back Ambisonics signals in combination with head tracking by the webcam is computationally demanding.

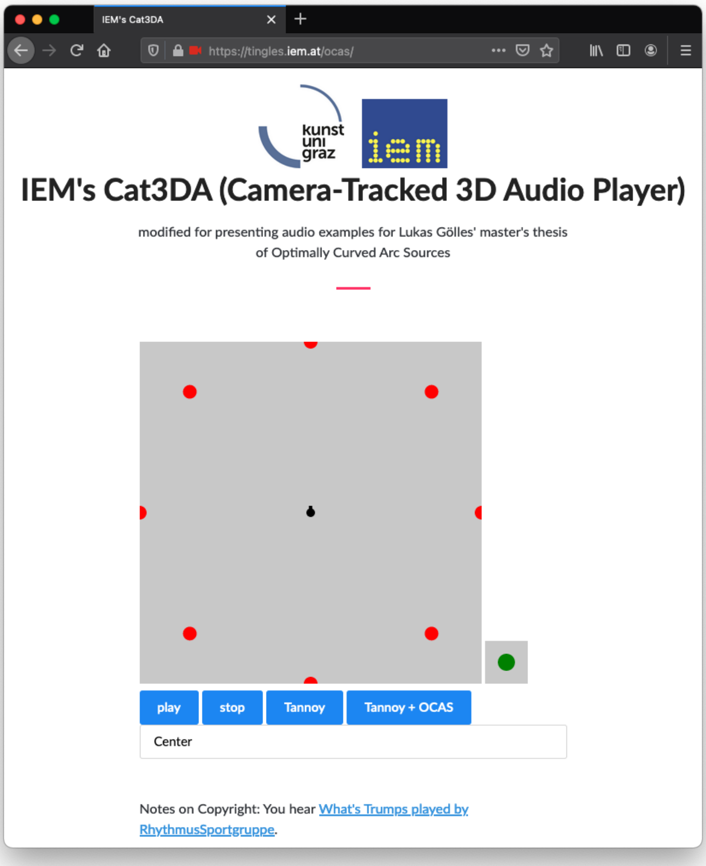

IEM's Cat3DA (Camera-Tracked 3D Audio Player)

modified for presenting audio examples for Lukas Gölles' master's thesis of Optimally Curved Arc Sources

Notes on Copyright: You hear What's Trumps played by RhythmusSportgruppe.

Figure 4.19 – Screenshot of the CAT3DA player.

---

[1] `https://tingles.iem.at/ocas/`

Chapter 5

Conclusion and Outlook

This thesis was able to present a novel source type in sound reinforcement that targets a constant direct-sound level (as an exemplary target). The resulting source type produces wave fronts emerging form an arc-shaped, linear contour or curve and is called Optimally Curved Arc Source (OCAS). This thesis discusses the theory behind the differential equation resulting from the stationary phase approximated integral of the Green's function. This differential equation contains expressions that depends on the geometry of the source, i.e. the first and second derivatives. With the wish of a direct-sound level which is independent of the listeners position this differential equation resulted. Chapter 2 gave also a solution approach beside ordinary differential equation solvers implemented in MATLAB or similar software tools. As the Euler Method is sufficient accurately by using a small step size and not computationally demanding, it allows to build a web-based solver, written in JavaScript[1].
OCAS implementations that do not target large-scale applications require solutions that are more compact than standard components. As a successful solution the thesis presented a waveguide design process and managed to prove the concept in measurement.

Chapter 3 outlined simulations based on placing multiple point sources along the OCAS contour. It was shown that the OCAS reaches flat coverage which is faded out for distant listeners. If an attenuation of $6\,\mathrm{dB}$ is defined as limit, the bigger part of the listening plane is provided with high-quality sound upon a critical frequency which depends on the OCAS size. In this chapter is was also shown that a slight misconfiguration, i.e. a small shift in the vertical axis, may improve the supply for distant listening positions at the expense on the level of nearer ones.
Chapter 3 moreover discussed the question whether line-source arrays offer useful ways of implementing the OCAS shape. As the stationary phase method is somewhat equivalent to setting up line source arrays in Soundvision, the section discussed also the usage of the OCAS contour with existing loudspeakers. A simple stereo sound reinforcement setup may be configured by discretizing the OCAS with line-source cabinets. Comparing to a point source, the OCAS coverage shows its strength, not only in the coverage, but also considering the mean absolute localisation error of the setup. Finally an OCAS 3D sound

---

[1] `https://lukas_goelles.iem.sh/ocas_web/`

reinforcement setup demonstrates the advantage of using the new source compared to point sources as the point source arrangement yielded approximately $44\,\%$ of the listening plane as plausible sweet area while the OCAS reached $75\,\%$.

Chapter 4 finally verifies the theory based on a compact prototype for medium-scale sound reinforcement at the IEM CUBE. Measurements with the waveguide confirmed the theoretical and simulated results. A virtualisation using the CAT3DA player gives interested readers the option of listening to a virtual setup[2] as a "preview" with the option to switch to an ordinary point-source loudspeaker.

Further work should consider modifying and psycho-acoustically optimizing the direct-sound target. Moreover, good strategies for designing wide-band OCAS systems are yet to be found.

---

[2] `https://tingles.iem.at/ocas/`

Appendix A

Mathematical Appendix

A.1 Integral of Green's Function over z

The sound pressure of a line source can be calculated by integration of the Green's function over the z axis,

$$\int_{-\infty}^{\infty} G(R,\omega)\,\mathrm{d}z\,. \tag{A.1}$$

In [17] the Hankel function zeroth order of second kind $H_0^{(2)}(k\,R)$ is defined by the integral $\frac{1}{\pi}\int_{-i\infty}^{i\infty} e^{-i\,k\,R\,\cos\alpha}\,\mathrm{d}\alpha$ (Sommerfeld integral for the Hankel function). To make it applicable, the transformation $z = -j\,R_0\,\sin\alpha$ is needed and the distance R is written as

$$R = \sqrt{x_r^2 + y_r^2 + z^2} = \sqrt{R_0^2 + z^2} = \sqrt{R_0^2 - R_0^2\,\sin^2\alpha} = R_0\,\cos\alpha\,, \tag{A.2}$$

so that the integral is rewritten and solved using the definition of the Hankel function,

$$\int_{-\infty}^{\infty} G(R,\omega)\,\mathrm{d}z = \frac{i}{4\,\pi}\int_{-i\infty}^{i\infty} e^{-i\,k\,R\,\cos\alpha}\,\mathrm{d}\alpha = \frac{1}{4\,i}\,H_0^{(2)}(k\,R)\,. \tag{A.3}$$

A.2 Derivatives: Distance

For solving the stationary phase approximated integral, the second derivative of the distance $R = \|\boldsymbol{x} - \boldsymbol{x}_r\| = \sqrt{[x - x_r]^2 + v(x)^2}$ inserted into the Green's Function is needed. By applying the chain rule, one gets the first derivative with respect to x,

$$R' = \frac{\mathrm{d}R}{\mathrm{d}x} = \frac{2\,(x - x_r) + 2\,v\,v'}{2\,\sqrt{((x - x_r)^2 + v^2}} = \frac{x - x_r + v\,v'}{R}\,. \tag{A.4}$$

For the second derivative, the chain rule and the division rule are needed,

$$\begin{aligned} R'' = \frac{\mathrm{d}^2 R}{\mathrm{d}x^2} &= \frac{R\,\left[1 + v\,v'' + (v')^2\right] - \frac{[x - x_r + v\,v']^2}{R}}{R^2} && \text{(A.5)} \\ &= \frac{R^2\,\left[1 + v\,v'' + (v')^2\right] - \left[x - x_r + v\,v'\right]^2}{R^3}\,. && \text{(A.6)} \end{aligned}$$

The stationary phase method claims that the first derivative of R gets 0, i.e. $x - x_r + v\,v' = 0$. Rearranging this equation yields a formula for calculating x_r

$$x_r = x + v\,v'\,, \tag{A.7}$$

and also a formula to replace $x - x_r$ in the second derivative of R,

$$x - x_R = -v\,v'\,. \tag{A.8}$$

The distance R and the second derivative at the stationary phase point $\boldsymbol{x}_s$ are written as

$$\begin{aligned} R\Big|_{\boldsymbol{x}_s} &= \sqrt{(-v\,v')^2 + (v')^2}\Big|_{\boldsymbol{x}_s} = v\,\sqrt{1 + (v')^2}\Big|_{\boldsymbol{x}_s} && \text{(A.9)} \\ R''\Big|_{\boldsymbol{x}_s} &= \frac{R^2\,\left[1 + v\,v'' + v'^2\right] - \left[-v\,v' + v\,v'\right]^2}{R^3}\Bigg|_{\boldsymbol{x}_s} && \text{(A.10)} \\ &= \frac{1 + v\,v'' + (v')^2}{R}\Bigg|_{\boldsymbol{x}_s}\,. && \text{(A.11)} \end{aligned}$$

A.3 Derivatives: Distance

For applying the stationary phase method for the two-dimensional integral, the second derivatives of the distance R with respect to s and φ are needed. By $R = \|\boldsymbol{x}_s - \boldsymbol{r}\| = \sqrt{(\boldsymbol{x}_s - \boldsymbol{r})^T\,(\boldsymbol{x}_s - \boldsymbol{r})} = \sqrt{x_r^2 + x^2 - 2\,x\,x_r\,\cos\varphi + v^2}$ the derivate of R is

$$\frac{\mathrm{d}R}{\mathrm{d}s} = \frac{-2\,\frac{\mathrm{d}\boldsymbol{r}^T}{\mathrm{d}s}\,(\boldsymbol{x}_r - \boldsymbol{r})}{2R} = -\frac{\boldsymbol{t}^T\,(\boldsymbol{x}_r - \boldsymbol{r})}{R} = 0, \tag{A.12}$$

$$\frac{\mathrm{d}R}{\mathrm{d}\varphi} = \frac{x\,x_r\,\sin\varphi}{R} = 0, \qquad \Longrightarrow\ \varphi = 0, \tag{A.13}$$

and the second-order derivatives are

$$\frac{\mathrm{d}^2R}{\mathrm{d}s^2} = \frac{\boldsymbol{t}^T\,\boldsymbol{t} - \kappa\,\boldsymbol{n}^T(\boldsymbol{x}_r - \boldsymbol{r})}{R} + \cancel{\frac{\boldsymbol{t}^T(\boldsymbol{x}_r - r)}{R^2}\,\frac{\boldsymbol{t}^T(\boldsymbol{x}_r - \boldsymbol{r})}{R}}\Bigg|_{\frac{\mathrm{d}R}{\mathrm{d}s}=0} \tag{A.14}$$

$$= \frac{1 + \kappa\,\|\boldsymbol{x}_s - \boldsymbol{r}\|}{R_s} = \frac{1 + \kappa\,R_s}{R_s}$$

$$\frac{\mathrm{d}^2R}{\mathrm{d}\varphi^2} = \frac{x\,x_r\,\cos\varphi}{R}\Bigg|_{\frac{\mathrm{d}R}{\mathrm{d}\varphi}=0} = \frac{x_s\,x_r}{R_s}\,. \tag{A.15}$$

A.4 Relationship of the source curvature and the vertical parameter

To get differential equations out of the approximated integrals that depends on the curvature, the parameters has to be related to the vertical parameter v. Therefore the slope of a function $v(x)$ is considered,

$$\frac{\Delta v}{\Delta x} = \tan(\varphi) \qquad \lim_{\Delta x \to 0}\ \Longrightarrow\ v' = \tan(\varphi) \tag{A.16}$$

as well as the arc length,

$$\Delta s = \sqrt{\Delta x^2 + \Delta v^2}, \tag{A.17}$$

$$\frac{\Delta s}{\Delta x} = \sqrt{1 + \left(\frac{\Delta v}{\Delta x}\right)^2} \qquad \lim_{\Delta x \to 0}\ \Longrightarrow\ \sqrt{1 + v'^2} = s'\,. \tag{A.18}$$

Further it is known that

$$\Delta s \approx \rho\,\Delta\varphi \tag{A.19}$$

$$\frac{\Delta s}{\Delta x} \approx \rho\,\frac{\Delta\varphi}{\Delta x} \qquad \lim_{\Delta x \to 0}\ \Longrightarrow\ s' = \rho\,\varphi' = \rho\,\frac{v''}{1 + v'^2}\,, \tag{A.20}$$

that allows to equalize both expressions for s',

$$\sqrt{1 + v'^2} = \rho\,\frac{v''}{1 + v'^2}\,, \tag{A.21}$$

so that the curvature becomes,

$$\kappa = \frac{1}{\rho} = \frac{v''}{\sqrt{\left(1 + v'^2\right)^3}} \,. \tag{A.22}$$

A.5 Rotation around an arbitrary axis

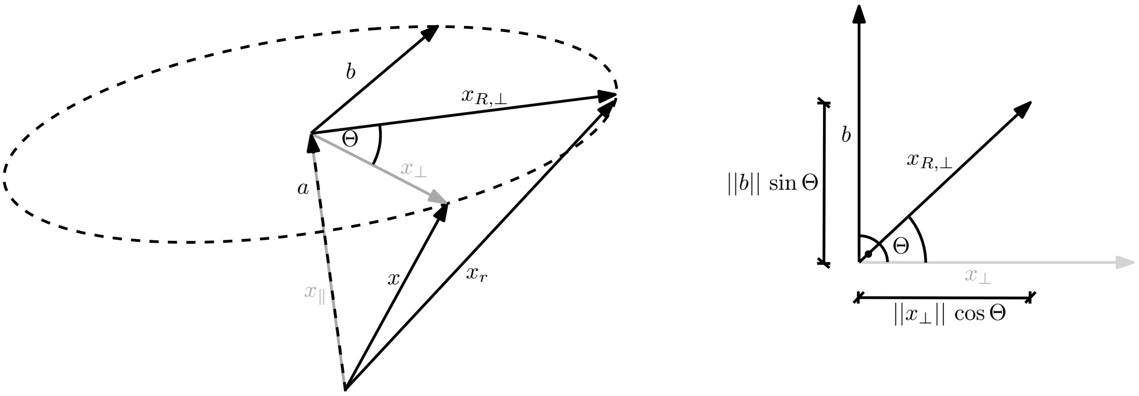

Figure A.1 – Rotation around arbitrary axis $\boldsymbol{a}$

Figure A.1 shows the geometry to rotate a vector $\boldsymbol{x}$ around an arbitrary axis $\boldsymbol{a}$ by the angle Θ as derived in [46]. For simplicity it is assumed that $\boldsymbol{a}$ passes the origin. First it has to be ensured that the vector, which describes the rotation axis, is a unit vector,

$$\boldsymbol{a}_0 = \frac{\boldsymbol{a}}{||\boldsymbol{a}||} \,. \tag{A.23}$$

The vector $\boldsymbol{x}$ is now decomposed into a parallel component to the rotation axis $\boldsymbol{x}_\parallel$ and an orthogonal component $\boldsymbol{x}_\perp$,

$$\boldsymbol{x}_\parallel = \left(\boldsymbol{x}^T \boldsymbol{a}_0\right) \boldsymbol{a}_0 \qquad\qquad \boldsymbol{x}_\perp = \boldsymbol{x} - \boldsymbol{x}_\parallel \,. \tag{A.24}$$

The rotated vector $\boldsymbol{x}_R$ is found by $\boldsymbol{x}_\parallel$ and $\boldsymbol{x}_{R,\perp}$,

$$\boldsymbol{x}_R = \boldsymbol{x}_\parallel + \boldsymbol{x}_{R,\perp} \,. \tag{A.25}$$

As the parallel component is already calculated in equation (A.24), only $\boldsymbol{x}_{R,\perp}$ has to be expressed by the known parameters. The cross product of $\boldsymbol{x}_\perp$ and $\boldsymbol{a}_0$ seems to be helpful in the next step,

$$\boldsymbol{b} = \boldsymbol{x}_\perp \times \boldsymbol{a}_0 = \left(\boldsymbol{x} - \boldsymbol{x}_\parallel\right) \times \boldsymbol{a}_0 = \boldsymbol{x} \times \boldsymbol{a}_0 - \underbrace{\boldsymbol{x}_\parallel \times \boldsymbol{a}_0}_{=0} \,. \tag{A.26}$$

The orthogonal component of the rotated vector $\boldsymbol{x}_{R,\perp}$ is expressed by using the geometry of the rectangular triangle shown in Figure A.1 on the right side,

$$\boldsymbol{x}_{R,\perp} = \boldsymbol{x}_\perp \cos\Theta + \boldsymbol{b}\sin\Theta = \left(\boldsymbol{x} - \left[\boldsymbol{x}^T \boldsymbol{a}_0\right] \boldsymbol{a}_0\right) \cos\Theta + \left(\boldsymbol{x} \times \boldsymbol{a}_0\right) \sin\Theta \,. \tag{A.27}$$

Inserting the properties for $\boldsymbol{x}_{\|}$ and $\boldsymbol{x}_{R,\perp}$ into equation (A.25) yields

$$\begin{aligned}
\boldsymbol{x}_R &= \left(\boldsymbol{x}^T \boldsymbol{a}_0\right) \boldsymbol{a}_0 + \boldsymbol{x}_\perp \cos\Theta + (\boldsymbol{x} \times \boldsymbol{a}_0) \sin\Theta && \text{(A.28)}\\
&= \left(\boldsymbol{x}^T \boldsymbol{a}_0\right) \boldsymbol{a}_0 + \boldsymbol{x} \cos\Theta - \left(\boldsymbol{x}^T \boldsymbol{a}_0\right) \boldsymbol{a}_0 \cos\Theta + (\boldsymbol{x} \times \boldsymbol{a}_0) \sin\Theta && \text{(A.29)}\\
&= (1-\cos\Theta) \left(\boldsymbol{x}^T \boldsymbol{a}_0\right) \boldsymbol{a}_0 + \boldsymbol{x} \cos\Theta + (\boldsymbol{x} \times \boldsymbol{a}_0) \sin\Theta && \text{(A.30)}
\end{aligned}$$

To define a rotation matrix, all products have to be expanded,

$$\begin{aligned}
\left(\boldsymbol{x}^T \boldsymbol{a}_0\right) \boldsymbol{a}_0 &= \left(\begin{bmatrix} x_x & x_y & x_z \end{bmatrix} \begin{bmatrix} a_{0,x} \\ a_{0,y} \\ a_{0,z} \end{bmatrix}\right) \begin{bmatrix} a_{0,x} \\ a_{0,y} \\ a_{0,z} \end{bmatrix} && \text{(A.31)}\\
&= \begin{bmatrix} x_x\, a_{0,x}^2 & x_x\, a_{0,x}\, a_{0,y} & x_x\, a_{0,x}\, a_{0,z} \\ x_y\, a_{0,x}\, a_{0,y} & x_y\, a_{0,y}^2 & x_y\, a_{0,y}\, a_{0,z} \\ x_z\, a_{0,y}\, a_{0,z} & x_z\, a_{0,x}\, a_{0,z} & x_z\, a_{0,z}^2 \end{bmatrix} && \text{(A.32)}\\
&= \begin{bmatrix} a_{0,x}^2 & a_{0,x}\, a_{0,y} & a_{0,x}\, a_{0,z} \\ a_{0,x}\, a_{0,y} & a_{0,y}^2 & a_{0,y}\, a_{0,z} \\ a_{0,y}\, a_{0,z} & a_{0,x}\, a_{0,z} & a_{0,z}^2 \end{bmatrix} \boldsymbol{x} && \text{(A.33)}\\
\boldsymbol{x} \times \boldsymbol{a}_0 &= \begin{bmatrix} x_x \\ x_y \\ x_z \end{bmatrix} \times \begin{bmatrix} a_{0,x} \\ a_{0,y} \\ a_{0,z} \end{bmatrix} = \begin{bmatrix} x_y\, a_{0,z} - x_z\, a_{0,y} \\ x_z\, a_{0,x} - x_x\, a_{0,z} \\ x_x\, a_{0,y} - x_y\, a_{0,x} \end{bmatrix} && \text{(A.34)}\\
&= \begin{bmatrix} 0 & -a_{0,z} & a_{0,y} \\ a_{0,z} & 0 & -a_{0,x} \\ -a_{0,y} & a_{0,x} & 0 \end{bmatrix} \boldsymbol{x}\,. && \text{(A.35)}
\end{aligned}$$

With this quantities the rotated vector gets

$$\boldsymbol{x}_R = \left[(1-\cos\Theta) \begin{bmatrix} a_{0,x}^2 & a_{0,x}\, a_{0,y} & a_{0,x}\, a_{0,z} \\ a_{0,x}\, a_{0,y} & a_{0,y}^2 & a_{0,y}\, a_{0,z} \\ a_{0,y}\, a_{0,z} & a_{0,x}\, a_{0,z} & a_{0,z}^2 \end{bmatrix} + \boldsymbol{I} \cos\Theta + \begin{bmatrix} 0 & -a_{0,z} & a_{0,y} \\ a_{0,z} & 0 & -a_{0,x} \\ -a_{0,y} & a_{0,x} & 0 \end{bmatrix} \sin\Theta\right] \boldsymbol{x}\,. \tag{A.36}$$

Defining the expression inside the braces as rotation matrix $\boldsymbol{R}_a$ it becomes

$$\boldsymbol{R}_a = \begin{bmatrix} (1-\cos\Theta)\, a_{0,x}^2 + \cos\Theta & (1-\cos\Theta)\, a_{0,x}\, a_{0,y} + \cos\Theta - a_{0,z} \sin\Theta & (1-\cos\Theta)\, a_{0,y}\, a_{0,z} + \cos\Theta + a_{0,y} \sin\Theta \\ (1-\cos\Theta)\, a_{0,x}\, a_{0,y} + \cos\Theta + a_{0,z} \sin\Theta & (1-\cos\Theta)\, a_{0,y}^2 + \cos\Theta & (1-\cos\Theta)\, a_{0,x}\, a_{0,y} + \cos\Theta - a_{0,x} \sin\Theta \\ (1-\cos\Theta)\, a_{0,x}\, a_{0,z} + \cos\Theta - a_{0,y} \sin\Theta & (1-\cos\Theta)\, a_{0,y}\, a_{0,z} + \cos\Theta + a_{0,x} \sin\Theta & (1-\cos\Theta)\, a_{0,z}^2 + \cos\Theta \end{bmatrix} \tag{A.37}$$

so that $\boldsymbol{x}_R = \boldsymbol{R}\,\boldsymbol{x}$.

Appendix B

JavaScript: Numerical Solution

```
// initialize parameters
var v = [];      // vertical axis
var v1 = [];     // first derivative
var g = 10;      // curvature parameter
var xstart = 0;
var xend = 1;
var cardinality = 1000;

var x = makeArr(xstart, xend, cardinality); // equivalent to Matlab's linspace
var v0 = 1;   // default initialization v(0)
var v10 = 0;  // default initialization v'(0)

v[0] = 1;
v1[0] = 0;
// solve ODE by Euler's method
var xr = [];
for (let ii = 0; ii < x.length - 1; ii++) {
  v[ii + 1] = v[ii] + (x[ii + 1] - x[ii]) * v1[ii];
  v1[ii + 1] = v1[ii] + (x[ii + 1] - x[ii]) * feval(v[ii], v1[ii], g);
  xr[ii+1] = x[ii+1]+v[ii+1]*v1[ii+1];
};
// discretize
var distance = [];
var index = v.length-1;
var xSD = [];
var vSD = [];
var xrD = [];
var height = 0.1;
for(var jj = 0; jj < 10000;jj++){
  xtemp = x[index];
  vtemp = v[index];
  distance=[];
  for(var ll = 0; ll < index;ll++){
    distance[ll] = Math.abs(Math.pow(Math.pow(xtemp-x[ll],2)+Math.pow(vtemp-v[ll],2),0.5)-height);
```

```
  }
  index = distance.indexOf(Math.min(...distance));
  if (x[index] <= 0) {
      break;
  }
  xSD[index] = x[index];
  vSD[index] = v[index];
  xrD[index] = xr[index];
}

// append first data point

xSD[x.length-1] = x[x.length-1];
vSD[x.length-1] = v[x.length-1];
xrD[x.length-1] = xr[x.length-1];

// differential equation as own function
function feval(v, v1, g) {
  return g * Math.sqrt(1 + Math.pow(v1, 2)) / Math.pow(v, 2) - 1 / v - Math.pow(v1, 2) / v;
}
```

Listing B.1 – Relevant JavaScript Code for solving the differential equation by Euler's Method

Bibliography

[1] B. Manor, “Thoughts and Ideas behind the design of Line arrays,” online. [Online]. Available: http://www.burton-manor.co.uk/index.php/legacy/1-thoughts-and-ideas-behind-the-design-of-line-arrays

[2] F. Toole, *Sound Reproduction: The Acoustics and Psychoacoustics of Loudspeakers and Rooms* . Elsevier Ltd, 2008.

[3] C. Heil and M. Urban, “Sound Fields Radiated By Multiple Sound Sources Arrays,” march 1992.

[4] M. Urban, C. Heil, and P. Bauman, “Wavefront Sculpture Technology,” in *Journal of the Audio Engineering Society. Audio Engineering Society*, vol. 51, 10 2003.

[5] D. L. Smith, “Discrete-Element Line Arrays-Their Modeling and Optimization,” in *Journal of the Audio Engineering Society*, vol. 45, no. 11, 1997, pp. 949–964. [Online]. Available: http://www.aes.org/e-lib/browse.cfm?elib=7835

[6] F. Straube, F. Schultz, M. Makarski, S. Spors, and S. Weinzierl, “Evaluation Strategies for the Optimization of Line Source Arrays,” in *Journal of the Audio Engineering Society*, vol. 2015, 07 2015.

[7] F. Straube, D. Albanés, F. Schultz, and S. Weinzierl, “Zur Optimierung der Krümmung von Line Source Arrays,” in *Fortschritte der Akustik - DAGA*, 03 2017.

[8] C. Heil, “Sound wave guide,” U.S. Patent 5163167A, Oct. 1992.

[9] E. Vincenot and F. Deffarges, “Sound-Producing Device With Acoustic Waveguide,” U.S. Patent 6585077B2, Jul. 2003.

[10] J. Spillmann and S. P. Riemersma, “Acoustic Waveguide,” U.S. Patent US 957923B2, Feb. 2017.

[11] S. Desrosiers, G. P. McKinnon, and Z. Zuo, “Isophasic Waveguide for a Loudspeaker,” U.S. Patent US 2020/02, Jul. 2020.

[12] M. Frank, “Phantom Sources using Multiple Loudspeakers in the Horizontal Plane,” Ph.D. dissertation, University of Music and Performing Arts Graz, 2013. [Online]. Available: http://phaidra.kug.ac.at/o:7008

[13] F. Zotter and M. Frank, *Ambisonics: A Practical 3D Audio Theory for Recording, Studio Production, Sound Reinforcement, and Virtual Reality*, 01 2019.

[14] M. Blochberger, F. Zotter, and M. Frank, “Sweet area size for the envelopment of a recursive and a non-recursive diffuseness rendering approach,” in *Proceedings of 5th International Conference on Spatial Audio ICSA*, Nov. 2019. [Online]. Available: https://www.db-thueringen.de/receive/dbt_mods_00039969

[15] L. Gölles, V. Drack, F. Zotter, and M. Frank, “Influence of horizontal loudspeaker layout geometry on sweet area shape for widened/diffuse frontal sound,” in *Proceedings of 148th AES Convention*, 06 2020.

[16] J. Nettingsmeier and P. Maier, “Scaling up: Making point-source multichannel material work for large listening areas,” in *Proceedings of 3rd International Conference on Spatial Audio ICSA*, 01 2015.

[17] E. Skudrzyk, *The Foundations of Acoustics: Basic Mathematics and Basic Acoustics*, 1971.

[18] Encyclopedia of Mathematics, “Method Of The Stationary Phase,” Jun. 2020, accessed at 17.01.2021. [Online]. Available: https://encyclopediaofmath.org/wiki/Stationary_phase,_method_of_the

[19] J. C. Butcher, “Numerical methods for ordinary differential equations,” 2008.

[20] J. D’Errico, “arclength - A Matlab function,” 2020. [Online]. Available: https://de.mathworks.com/matlabcentral/fileexchange/34871-arclength

[21] B. McDonald, “surf2stl - A Matlab function,” 2020. [Online]. Available: https://de.mathworks.com/matlabcentral/fileexchange/4512-surf2stl

[22] “ÖVE/ÖNORM EN 61672-1: Electroacoustics – Sound level meters, Part 1: Specifications,” Austrian Standards Institute, Vienna, AT, Standard, Jan. 2015.

[23] Nexo, “NS 1 v3.3,” Dec. 2020. [Online]. Available: https://nexo-sa.com/software-update/doc/ns1/#!/en

[24] L’Acoustics, “KARA II - long throw line source manual,” Apr. 2020, accessed at 05.02.2021. [Online]. Available: https://www.l-acoustics.com/wp-content/uploads/2020/01/kara_ii_sp_en_1-0.pdf

[25] ——, “Soundvision 3.3.0,” Dec. 2020. [Online]. Available: https://www.l-acoustics.com/en/software/soundvision-presentation/

[26] P. Stitt, S. Bertet, and M. Van Walstijn, “Extended Energy Vector Prediction of Ambisonically Reproduced Image Direction at Off-Center Listening Positions,” pp. 299–310, 05 2016.

[27] E. Kurz and M. Frank, “Prediction of the listening area based on the energy vector,” in *Proceedings of ICSA 2017*, 09 2017.

[28] B. Rakerd, W. Hartmann, and J. Hsu, “Echo suppression in the horizontal and median sagittal planes,” in *The Journal of the Acoustical Society of America*, vol. 107, 03 2000, pp. 1061–4.

[29] Institute of Electronic Music and Acoustics, University of Music and Performing Arts Graz, “Student 3D Audio Production Competition,” 2020. [Online]. Available: https://ambisonics.iem.at/s3dapc

[30] F. Zotter, H. Pomberger, and M. Noisternig, “Energy-Preserving Ambisonic Decoding,” in *Acta Acustica united with Acustica*, vol. 98, 01 2012, pp. 37–47.

[31] M. Frank, “How to make Ambisonics sound good,” in *Proceedings of Forum Acusticum*, 09 2014.

[32] M. Frank and F. Zotter, “Exploring the perceptual sweet area in Ambisonics,” in *Proceedings of the AES 142nd Convention (AES 142nd Convention)*, 05 2017.

[33] Prusa Research, “Prusa I3 MK3S+ 3D printer,” 2020. [Online]. Available: https://www.prusa3d.com/original-prusa-i3-mk3/

[34] SB-Audience, “BIANCO-44CD-T compression driver, data sheet,” 2020. [Online]. Available: https://lautsprechershop.de/pdf/sbaudience/Bianco-44CD-T.pdf

[35] F. Wendt, F. Zotter, M. Frank, and R. Höldrich, “Correction: Wendt, f.; et al. auditory distance control using a variable-directivity loudspeaker. appl. sci. 2017, 7, 666,” in *Applied Sciences*, vol. 7, no. 11, 2017. [Online]. Available: https://www.mdpi.com/2076-3417/7/11/1174

[36] H. Chen, P. Samarasinghe, T. Abhayapala, and W. Zhang, “Estimation of the direct-to-reverberant Energy Ratio using a spherical microphone array,” in *Proceedings of the ACE Challenge Workshop - a satellite event of IEEE-WASPAA 2015*, 10 2015.

[37] L. Gölles and F. Zotter, “Directional Enhancement of First-Order Ambisonic Room Impulse Responses By The 2+2 Directional Signal Estimator,” in *Proceedings of the 15th International Converence on Audio Mostly*, 09 2020.

[38] L. Gölles, R. Höldrich, F. Zotter, and M. Frank, “Camera Tracked 3D Audio player,” online, 2020. [Online]. Available: https://git.iem.at/lukas_goelles/cat3da

[39] Google, “MediaPipe Face Mesh ,” 2020. [Online]. Available: https://google.github.io/mediapipe/solutions/face_mesh.html

[40] Dash Industry Forum, “MPEG-DASH,” 2015. [Online]. Available: https://github.com/Dash-Industry-Forum/dash.js/wiki

[41] A. Politis and D. Poirier-Quinot, “JSAmbisonics,” 2017. [Online]. Available: https://github.com/polarch/JSAmbisonics

[42] Deutsche Gesellschaft für Akustik, “Stimulus-Datenbank: Jazz/Funk „Rhythmussportgruppe“: What’s Trumps,” accessed 18.02.2021. [Online]. Available: https://www.dega-akustik.de/va/stimulus-datenbank

[43] D. Rudrich, “IEM Plugin Suite,” 2020, accessed 18.02.2021. [Online]. Available: https://plugins.iem.at

[44] M. Kronlachner, “mcfx Plugin Suite,” accessed 18.02.2021. [Online]. Available: http://www.matthiaskronlachner.com/?p=1910

[45] C. Schörkhuber, M. Zaunschirm, and R. Höldrich, “Binaural Rendering of Ambisonic Signals via Magnitude Least Squares,” in *Fortschritte der Akustik - DAGA*, 03 2018.

[46] E. Lengyel, *Mathematics for 3D Game Programming and Computer Graphics*, 3rd ed., ser. Game development series, 2012.